STRUCTURAL, ELECTRONIC, AND PHOTOCATALYTIC PROPERTIES OF Ce-DOPED $PbBi_2Nb_2O_9$ UNDER SOLAR SIMULATION IRRADIATION

RACHANON KLONDON

A Thesis Submitted in Partial Fulfillment of the Requirements for the
Degree of Doctor of Philosophy in Chemistry
Suranaree University of Technology
Academic Year 2025

สมบัติเชิงโครงสร้าง เชิงอิเล็กทรอนิกส์ และสมบัติโฟโตคะตะไลติกของซีเรียมที่เติมลงในสารประกอบ $PbBi_2Nb_2O_9$ ภายใต้การฉายแสงอาทิตย์จำลอง

นายรชานนท์ กลอนดอน

วิทยานิพนธ์นี้เป็นส่วนหนึ่งของการศึกษาตามหลักสูตรปริญญาวิทยาศาสตรดุษฎีบัณฑิต
สาขาวิชาเคมี
มหาวิทยาลัยเทคโนโลยีสุรนารี
ปีการศึกษา 2568

STRUCTURAL, ELECTRONIC, AND PHOTOCATALYTIC PROPERTIES OF Ce-DOPED $PbBi_2Nb_2O_9$ UNDER SOLAR SIMULATION IRRADIATION

Suranaree University of Technology has approved this thesis submitted in partial fulfillment of the requirements for the Degree of Doctor of Philosophy.

Thesis Examining Committee

Suttipong Wannapaiboon

(Dr. Suttipong Wannapaiboon)
Chairperson

Theeranun Siritanon

(Assoc. Prof. Dr. Theeranun Siritanon)
Member (Thesis Advisor)

(Prof. Dr. Jatuporn Wittayakun)
Member

(Assoc. Prof. Dr. Sanchai Prayoonpokarach)
Member

(Assoc. Prof. Dr. Phimphaka Harding)
Member

(Assoc. Prof. Dr. Yupaporn Ruksakulpiwat)
Acting Vice Rector for Academic Affairs
and Quality Assurance

(Prof. Dr. Santi Maensiri)
Acting Dean of Institute of Science

รชานนท์ กลอนดอน : สมบัติเชิงโครงสร้าง เชิงอิเล็กทรอนิกส์ และสมบัติโฟโตคะตะไลติกของซีเรียมที่เติมลงในสารประกอบ $PbBi_2Nb_2O_9$ ภายใต้การฉายแสงอาทิตย์จำลอง (STRUCTURAL, ELECTRONIC, AND PHOTOCATALYTIC PROPERTIES OF Ce-DOPED $PbBi_2Nb_2O_9$ UNDER SOLAR SIMULATION IRRADIATION) อาจารย์ที่ปรึกษา : รองศาสตราจารย์ ดร.ธีรนันท์ ศิริตานนท์, 70 หน้า

คำสำคัญ: โฟโตคะตะไลซิส เพอรอฟสไกต์แบบชั้นโครงสร้างชนิด Auvillius เลดบิทมัสไนโอเบียมออกไซด์ การเติมซีเรียม โฟโตคะตะลิสต์ที่ขับเคลื่อนด้วยแสงที่ตามองเห็นได้ การฉายแสงอาทิตยืจำลอง การแยกตัวของพาหะประจุ การย่อยสลายเมทิลีนบลู

โฟโตคะตะไลซิสเป็นวิธีการที่มีศักยภาพในการแก้ไขปัญหามลพิษทางสิ่งแวดล้อมโดยอาศัยการใช้พลังงานแสงอาทิตย์ โดยวัสดุ Aurivillius ได้รับความสนใจเป็นอย่างมาก เนื่องจากมีความเสถียรทางโครงสร้าง คุณสมบัติทางอิเล็กทรอนิกส์ที่สามารถปรับแต่งได้ และศักยภาพในการประยุกต์ใช้งานภายใต้แสงที่ตามองเห็นได้ งานวิจัยนี้มุ่งเน้นการสังเคราะห์และศึกษาวัสดุโฟโตคะตะลิสต์ $PbBi_2Nb_2O_9$ (PBNO) และ $PbBi_{2-x}Ce_xNb_2O_9$ ที่เติมซีเรียม (x = 0.00-0.50) เพื่อเพิ่มประสิทธิภาพการเร่งปฏิกิริยาด้วยแสงสำหรับการย่อยสลายสีย้อมอินทรีย์ภายใต้การฉายแสงอาทิตย์จำลอง จากการเปรียบเทียบวิธีการสังเคราะห์ที่แตกต่างกัน พบว่าวัสดุ PBNO ที่ได้จากวิธีโซล–เจลแสดงประสิทธิภาพโฟโตคะตะไลติกสูงที่สุด ซึ่งสามารถอธิบายได้จากลักษณะความพรุน พื้นที่ผิวจำเพาะที่สูง และโครงสร้างที่อุดมไปด้วยตำหนิบกพร่อง จากการปรับความเหมาะสมของอุณหภูมิการเผาพบว่า โครงสร้าง PBNO ที่เป็นเฟสเดียวได้มาจากการเผาที่อุณหภูมิ 750 °C การเติมซีเรียมในระดับปานกลาง (x = 0.20) สามารถรวมตัวอยู่ในโครงผลึก PBNO ได้อย่างมีประสิทธิภาพ ส่งผลให้เกิดการบิดเบือนของโครงสร้างผลึก การแคบลงของช่องว่างแถบพลังงาน การดูดกลืนแสงในช่วงที่ตามองเห็นได้ และการแยกตัวของพาหะประจุที่ดีขึ้น ผ่านพฤติกรรมรีดอกซ์ Ce^{3+}/Ce^{4+} โดยไม่ส่งผลต่อสถานะออกซิเดชันของ Pb^{2+}, Bi^{3+} และ Nb^{5+} จากผลการทดสอบประสิทธิภาพของกระบวนการโฟโตคะตะไลติกพบว่าวัสดุ $PbBi_{1.8}Ce_{0.2}Nb_2O_9$ แสดงกิจกรรมโฟโตคะตะไลติกสูงที่สุด โดยให้ประสิทธิภาพการย่อยสลายสูงกว่าวัสดุ PBNO บริสุทธิ์ประมาณ 2.6 เท่า และมีเสถียรภาพในการใช้งานซ้ำที่ดี การทดลองดักจับปัจจัยที่มีผลต่อปฏิกิริยาและการวิเคราะห์ตำแหน่งขอบแถบพลังงานระบุว่า โฮลที่เกิดจากแสงและอนุมูลไฮดรอกซิลเป็นชนิดที่มีบทบาทสำคัญที่สุดในกระบวนการย่อยสลาย

สาขาวิชาเคมี ลายมือชื่อนักศึกษา _____

ปีการศึกษา 2568 ลายมือชื่ออาจารย์ที่ปรึกษา _____

RACHANON KLONDON : STRUCTURAL, ELECTRONIC, AND PHOTOCATALYTIC PROPERTIES OF Ce-DOPED $PbBi_2Nb_2O_9$ UNDER SOLAR SIMULATION IRRADIATION. THESIS ADVISOR : ASSOC. PROF. THEERANUN SIRITANON, Ph.D. 70 PP.

Keywords: Photocatalysis, Aurivillius-type layered perovskite, $PbBi_2Nb_2O_9$, Cerium doping, Visible-light-driven photocatalyst, Solar simulation irradiation, Charge carrier separation, Methylene blue degradation

Photocatalysis is a promising approach for addressing environmental pollution using solar energy, with Aurivillius-type layered perovskite oxides attracting attention due to their structural stability, tunable electronic properties, and potential for visible-light-driven applications. In this work, $PbBi_2Nb_2O_9$ (PBNO) and cerium-doped $PbBi_{2-x}Ce_xNb_2O_9$ (x = 0.00-0.50) photocatalysts were synthesized to enhance photocatalytic performance for organic dye degradation under simulated solar irradiation. Among different synthesis routes (Sol–gel, Hydrothermal, and Molten salt methods), Sol–gel-derived PBNO exhibited superior photocatalytic activity despite its lower crystallinity, which was attributed to its porous morphology, higher surface area, and defect-rich structure. Optimization of calcination temperature revealed that a single-phase PBNO structure was achieved at 750 °C. Moderate Ce doping (x = 0.20) was effectively incorporated into the PBNO lattice, including lattice distortion band gap narrowing, enhanced visible-light absorption, and improved charge carrier separation through Ce^{3+}/Ce^{4+} redox behavior, without altering the oxidation states of Pb^{2+}, Bi^{3+} and Nb^{5+}. As a result, $PbBi_{1.8}Ce_{0.2}Nb_2O_9$ photocatalyst exhibited the highest photocatalytic performance, achieving approximately 2.6 times higher methylene blue degradation efficiency than pristine PBNO and demonstrating excellent cycling stability. Reactive species trapping experiments and band edge analysis identified photogenerated holes and hydroxyl radicals as the dominant active species in the degradation process.

School of Chemistry
Academic Year 2025

Student's Signature _____
Advisor's Signature _____

ACKNOWLEDGEMENT

First and foremost, I would like to express my deepest gratitude to my advisor, Assoc. Prof. Dr. Theeranun Siritanon, for her invaluable guidance, continuous support, and encouragement throughout this research. Her insight, patience, and expertise have been instrumental in shaping this work and my academic development.

I would also like to sincerely thank my collaborators, Assoc. Prof. Dr. Suwit Suthirakun and Mr. Panupol Untarabut, for their generous support and valuable contributions to the computational aspects of this thesis. My special appreciation goes to Dr. Suttipong Wannapaiboon for his kindness and guidance in allowing me to access and utilize advanced techniques at the Synchrotron Light Research Institute. His support opened an important opportunity that greatly enriched this research.

I am deeply thankful to my colleagues, Dr. Anurak Waehayee and Miss. Praphaiphon Phonsuksawang, for their friendship, encouragement, and insightful suggestions. Their support and thoughtful feedback have been invaluable, and I am truly fortunate to have shared this journey with them.

I am grateful to Suranaree University of Technology for providing the facilities and resources necessary to carry out this study. I would also like to acknowledge the financial support for OROG, which made this research possible.

Special thanks are extended to my colleagues and friends at Solid State Chemistry Laboratory and Computational Material Science and Catalysis group for their support, collaboration, and for creation a stimulating and friendly working environment.

Finally, I would like to express my deepest appreciation to my family for their unconditional love, understanding, and unwavering support throughout my journey. Their encouragement has been my greatest source of strength.

Rachanon Klondon

CONTENTS

Page

ABSTRACT IN THAI.....I
ABSTRACT IN ENGLISH.....II
ACKNOWLEDGEMENT.....III
CONTENTS.....IV
LIST OF TABLES.....VI
LIST OF FIGURES.....VII
CHAPTER
I INTRODUCTION 1
1.1 Significance of the study.....1
1.2 Photocatalysis.....3
1.3 Photocatalyst.....6
1.4 Perovskite material.....7
1.5 Sol-Gel method.....9
1.5.1 The basic steps in the Sol-Gel process.....9
1.5.2 The key advantages of the Sol-Gel method.....9
1.6 Doping photocatalyst.....10
1.7 Reference.....11
II LITERATURE REVIEWS.....15
2.1 $Pb_2Nb_2O_9$ photocatalyst.....15
2.2 Modified $Pb_2Nb_2O_9$ photocatalysts.....17
2.3 Modified photocatalyst by Ce-doping.....19
2.4 References.....23
III EXPERIMENTAL SECTION.....25
3.1 Materials and reagents.....25
3.2 Sample preparation.....25
3.3 Characterizations.....26

CONTENTS (Continued)

Page

3.3.1 X-ray diffraction (XRD) and structure refinement....26
3.3.2 Scanning electron microscopy (SEM) and Energy dispersive X-ray spectroscopy (EDX)....26
3.3.3 X-ray photoelectron spectroscopy (XPS)....27
3.3.4 UV-Visible spectrophotometer....27
3.3.5 Photoluminescence (PL)....28
3.3.6 X-ray adsorption spectroscopy (XAS)....29
3.4 Photocatalytic test....30
3.5 Computational details....31
3.6 References....31
IV RESULTS AND DISCUSSION....33
4.1 Crystal structure....33
4.1.1 Different preparation method of $PbBi_2Nb_2O_9$....33
4.1.2 Sol-Gel method by various calcination temperature....36
4.2 Ce-doped....37
4.2.1 Crystal structure of Ce-doped obtained samples....37
4.2.2 Morphology and surface area....43
4.2.3 Electronic band structure and band gap energy....46
4.2.4 Chemical state....49
4.3 Photocatalytic activity....53
4.4 References....63
V CONCLUTIONS....68
CURRICULLUM VITAE....70

LIST OF TABLES

Table **Page**

4.1 Cell Parameters, Cell Volumes (V), and degree of distortion in terms of the orthorhombicity ratio (| (*a* - *b*) / (*a* + *b*) |).....39

4.2 Assignment of Raman active modes of $PbBi_{2-x}Ce_xNb_2O_9$.....40

4.3 TRPL fitted data of $PbBi_{2-x}Ce_xNb_2O_9$ (x=0.00 and x=0.02).....57

4.4 Band parameters estimated by the calculation of work function (ϕ) and the measurement of UV-vis absorption and XPS valence band spectroscopy.....61

LIST OF FIGURES

Figure		Page
1.1	Photocatalytic degradation process (a), e^- and h^+ recombination (b)	4
1.2	Perovskite structure illustrated for ABO_3	7
2.1	Schematic structure of $PbBi_2Nb_2O_9$	15
2.2	Mechanism for the photocatalytic reduction of 4-NA to PPD by Nanocrystalline $PbBi_2Nb_2O_9$	17
2.3	XRD patterns of as-prepared PBNO and PBFNO samples by solid-state reaction	18
2.4	The mechanism of methyl orange dye degradation over 0.1% Ce-doped TiO_2 under UV light irradiation	20
2.5	Band edge positions of (a) Pristine ZrO_2 and $MgZrO_3$ (b) Band alignment in case of $Ce^{4+/3+}$: $MgZrO_3$ NCs	21
2.6	Mechanistic diagram of TC degradation by BCFO-7	22
3.1	XANES and EXAFS region within XAS	29
4.1	XRD patterns of $PbBi_2Nb_2O_9$ at different preparation methods Sol-gel (a), Hydrothermal (b) and Molten salt (c)	34
4.2	SEM images of $PbBi_2Nb_2O_9$ at different preparation methods Sol-gel (a), Hydrothermal (b) and Molten salt (c)	35
4.3	Photocatalytic degradation of $PbBi_2Nb_2O_9$ at different preparation methods	35
4.4	XRD patterns of $PbBi_2Nb_2O_9$ at temperatures of 650℃, 700℃, 750℃ and 800℃	37
4.5	XRD patterns (a) and their close-up (b) of $PbBi_2Nb_2O_9$ (x = 0.00, 0.05, 0.20, and 0.50)	39
4.6	The fitted FT-Raman of $PbBi_{2-x}Ce_xNb_2O_9$ (x = 0.00, 0.05, 0.20, and 0.50)	40
4.7	The FT-Raman spectra (a), the calculated Nb–O bond lengths (b) and FT-IR spectra (c) of $PbBi_{2-x}Ce_xNb_2O_9$ (x = 0.00, 0.05, 0.20, and 0.50)	43
4.8	SEM (a and d), HRTEM (b and e), SAED pattern (c and f) of $PbBi_2Nb_2O_9$ and $PbBi_{1.8}Ce_{0.2}Nb_2O_9$, and EDS of $PbBi_{1.8}Ce_{0.2}Nb_2O_9$ (g1-g6)	45

LIST OF FIGURES (Continued)

Figure **Page**

4.9 Nitrogen adsorption-desorption isotherm and surface area of $PbBi_{2-x}Ce_xNb_2O_9$.....46

4.10 UV-vis absorption spectra (a) and Kubelka–Munk plot (b) of $PbBi_{2-x}Ce_xNb_2O_9$ (x = 0.00, 0.05, 0.20, and 0.50). The density of state (DOS) of (c) pure and (d) Ce-doped $PbBi_2Nb_2O_9$**.** The colour of obtained photocatalysts (e).....48

4.11 Projected electronic density of states (PDOS) of s and p orbital of Pb and Ce and crystal orbital Hamilton populations (COHP) for Pb-O and Pb_{Bi}-O of (a) pure and (b) Ce-doped $PbBi_2Nb_2O_9$.....49

4.12 XPS spectrum: (a) survey spectra, and high-resolution spectrum of (b) Ce 3d, (c) Bi 4*f*, (d) Pb 4*f*, (e) Nb 3d, and (f) O 1*s* of $PbBi_{2-x}Ce_xNb_2O_9$ (x = 0.00, and 0.20).....51

4.13 XANES spectrum: (a) Pb (L_3-edge), (b) Bi (L_3-edge), (c) Nb (L_3-edge) and (d) Ce (L_3-edge) of $PbBi_{2-x}Ce_xNb_2O_9$ (x = 0.00, 0.05, 0.20, and 0.50).....52

4.14 Photolysis and photocatalytic activity of $PbBi_2Nb_2O_9$ between pH7 and 12 (a), The photocatalytic activities (b) and the percentages of MB degradation and the rate constants of the apparent pseudo first order reaction (c) at pH12 of $PbBi_{2-x}Ce_xNb_2O_9$. Cycling experiment of the photocatalytic degradation MB on $PbBi_{1.8}Ce_{0.2}Nb_2O_9$ (d).....54

4.15 PL spectra of $PbBi_{2-x}Ce_xNb_2O_9$ (a) and TRPL spectra of $PbBi_2Nb_2O_9$ and $PbBi_{1.80}Ce_{0.20}Nb_2O_9$ (b).....57

4.16 Inhibition of MB photocatalytic degradation over $PbBi_{1.8}Ce_{0.2}Nb_2O_9$ in the presence of different scavengers and argon atmosphere relative to the degradation without scavengers and under air atmosphere.....58

4.17 XPS at valence band of (a) $PbBi_2Nb_2O_9$ and (b) $PbBi_{1.8}Ce_{0.2}Nb_2O_9$. Diagram of the band energy (c) of $PbBi_2Nb_2O_9$ and $PbBi_{1.8}Ce_{0.2}Nb_2O_9$.....61

4.18 Proposed schematic band structures and mechanism of MB photo-degradation over the $PbBi_{1.8}Ce_{0.2}Nb_2O_9$ photocatalyst.....63

CHAPTER I
INTRODUCTION

1.1 Significance of the study

As societies undergo industrialization and population growth, the demand for energy resources such as fossil fuels, including coal, oil, and natural gas, has been significantly increased. These resources have been extensively combusted for electricity generation, transportation, and various industrial processes. As a consequence, toxic gases released from industrial activities and vehicular emissions have been introduced into the atmosphere, contributing substantially to air pollution. This pollution has been associated with respiratory illnesses and other adverse health effects among populations residing in contaminated environments (Dockery and Pope, 1994; Organization, 2020). In parallel, the direct discharge of industrial effluents and organic waste into natural water bodies has been widely practiced, leading to severe water pollution. As a result, the prevalence of water-borne diseases has been increased, and access to clean and safe drinking water has been critically limited for millions of people worldwide (Organization, 2023; Schwarzenbach, Egli, Hofstetter, Von Gunten and Wehrli, 2010). In addition to air and water pollution, the continuous accumulation of carbon dioxide (CO_2) in the atmosphere has been identified as a major contributor to global warming and climate change. These phenomena have produced profound impacts on natural ecosystems, global climate patterns, and sea-level rise (Change, 2013). In recognition of the urgency of these environmental challenges, the period from 2021 to 2030 has been designated by the United Nations as the “Decade on Ecosystem Restoration.” This global initiative highlights the necessity of mitigating environmental degradation and restoring damaged ecosystems (Canton, 2021). Achieving ecological sustainability has therefore been identified as a critical global

challenge, requiring strategies that satisfy present societal needs while preserving the capacity of future generations to meet their own demands (Brundtland, 1987).

Among renewable energy sources, the Sun has been recognized as an abundant and powerful source of energy, with an energy output far exceeding current global consumption. Solar energy has been widely regarded as a key component in the transition toward sustainable and environmentally friendly energy systems. Solar radiation can be harvested through multiple technologies, including photovoltaic systems, which directly convert sunlight into electricity. In addition, photoelectrochemical and photocatalytic processes have been developed to utilize solar energy for applications such as water splitting, hydrogen production, and environmental remediation, including the degradation of organic pollutants (Fujishima and Honda, 1972; Hoffmann, Martin, Choi and Bahnemann, 1995; Irshad et al., 2022; Lewis and Nocera, 2006).

Photocatalysis is defined as a process in which a chemical reaction is accelerated by a catalyst under light irradiation, where light serves as the primary energy source (Fujishima et al., 1972). This process is governed by the interaction between incident photons and the photocatalyst material, which enables various chemical transformations to occur. In photocatalytic systems, a photocatalyst material plays a central role by absorbing photons and generating photogenerated electron–hole pairs. These charge carriers migrate to the surface of the photocatalyst, where they participate in redox (reduction–oxidation) reactions involving electron transfer, ultimately driving chemical conversions (Hoffmann et al., 1995). Photocatalysis has been widely investigated for a range of environmentally beneficial applications, including the degradation of water pollutants and the conversion of abundant and stable molecules such as H_2O, CO_2, and N_2 (Chong, Jin, Chow and Saint, 2010; Hisatomi, Kubota and Domen, 2014; Lewis et al., 2006). Through these processes, valuable products such as hydrogen gas (H_2), hydrocarbon fuels (e.g., methane and methanol), and ammonia (NH_3) can be produced. In particular, CO_2 reduction and nitrogen fixation via photocatalytic routes have been recognized as promising strategies for environmental remediation and sustainable chemical production (Chen, Shen, Guo and

Mao, 2010; Wang and Domen, 2019). Collectively, these applications represent viable approaches for environmental purification and resource sustainability.

However, many conventional photocatalysts exhibit high activity only under ultraviolet (UV) light irradiation, which imposes a significant limitation on practical applications due to the low UV fraction in natural solar radiation (Linsebigler, Lu and Yates Jr, 1995). Consequently, the development of photocatalytic materials capable of efficiently utilizing visible light has become a major research focus. Among the investigated materials, $PbBi_2Nb_2O_9$ has been identified as a promising visible-light-responsive photocatalyst. Its electronic structure can be effectively tuned through elemental substitution or doping, enabling enhanced photocatalytic performance for a wide range of applications (Zhang and Zhu, 2012; Zou, Ye, Sayama and Arakawa, 2001).

In this work, the photocatalytic activity of $PbBi_2Nb_2O_9$ was enhanced through cerium (Ce) doping. The primary objective of this study was to systematically investigate the effects of Ce incorporation on the crystal structure, electronic properties, and photocatalytic performance of $PbBi_2Nb_2O_9$ -based materials. Particular emphasis was placed on evaluating the photocatalytic degradation of methylene blue as a model reaction to elucidate the role of Ce doping in improving photocatalytic efficiency.

1.2 Photocatalysis

Photocatalysis is a chemical process in which a photocatalyst is employed to accelerate and facilitate chemical reactions under light irradiation. This process has attracted significant attention in the field of sustainable and green chemistry due to its strong potential for addressing environmental challenges, including water purification and the production of clean and renewable fuels (Fujishima et al., 1972; Hoffmann et al., 1995; Irshad et al., 2022).

Photocatalytic reactions are surface-driven processes that occur on the surface of the photocatalyst material. The fundamental photocatalytic mechanism begins with the absorption of photons by the photocatalyst. For effective initiation of photocatalytic reactions, the energy of the absorbed photons must be equal to or

greater than the band gap energy of the photocatalyst ($h\mathbf{V} \geq Eg$). Upon photon absorption, electrons are excited from the valence band to the conduction band, resulting in the formation of photogenerated electron–hole pairs (e^- and h^+). These charge carriers subsequently migrate to the surface of the photocatalyst, where they participate in redox reactions with adsorbed species, leading to the degradation of pollutants or other chemical transformations (Chen and Mao, 2007; Schneider et al., 2014). The overall photocatalytic degradation process is schematically illustrated in Figure 1.1.

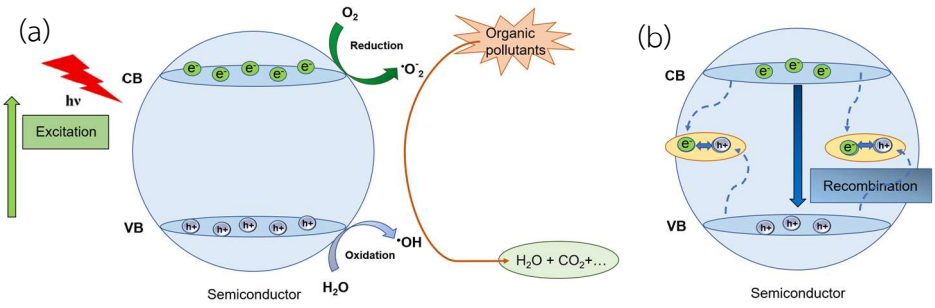


Figure 1.1 Photocatalytic degradation process (a), e^- and h^+ recombination (b).

The photogenerated electron–hole pairs are highly reactive species and serve as the key intermediates in photocatalytic reactions. Upon light irradiation, photoexcitation occurs when a semiconductor photocatalyst absorbs photons with energy equal to or greater than its band gap energy, resulting in the generation of free charge carriers, as expressed in Equation (1.1):

$$\text{Photocatalyst or Semiconductor} + h\mathbf{V} \longrightarrow h^+ + e^- \qquad (1.1)$$

Once generated, the electron–hole pairs are able to migrate to the surface of the photocatalyst, where they participate in a series of redox (reduction–oxidation) reactions with adsorbed species. The photogenerated electrons can react with molecular oxygen adsorbed on the catalyst surface, leading to the formation of superoxide radicals ($^{\bullet}O_2^-$) and hydroperoxyl radicals ($HOO^{\bullet}$), while the photogenerated

holes can oxidize either organic pollutants directly or surface-adsorbed water molecules and hydroxide ions to produce highly reactive hydroxyl radicals (•OH) (Kong, Yang, Rui and Ji, 2019). These elementary reactions are described in Equations (1.2) - (1.6):

$$e^- + O_2 \longrightarrow {}^\bullet O_2^- \qquad (O_2/{}^\bullet O_2^- = -0.33 \text{ eV at pH=7}) \qquad (1.2)$$

$${}^\bullet O_2^- + e^- \longrightarrow HOO^\bullet \qquad (O_2/HOO^\bullet = -0.05 \text{ eV, at pH=7}) \qquad (1.3)$$

$$h^+ + H_2O \longrightarrow {}^\bullet OH + H^+ \qquad ({}^\bullet OH/H_2O = 2.72 \text{ eV at pH=7}) \qquad (1.4)$$

$$h^+ + OH^- \longrightarrow {}^\bullet OH \qquad ({}^\bullet OH/OH^- = 1.89 \text{ eV at pH=7}) \qquad (1.5)$$

$$h^+ + \text{Organics} \longrightarrow \text{Intermediates}/CO_2 + H_2O \qquad (1.6)$$

In the context of photocatalytic degradation, the reactive oxygen species (ROS) generated on the photocatalyst surface subsequently react with dye molecules. Through these reactions, complex organic dye molecules are broken down into smaller intermediates and, in some cases, completely mineralized into CO_2 and H_2O, as illustrated in Equation (1.7):

$$\text{Dye molecules} + ({}^\bullet O_2^-, HOO^\bullet \text{ or } {}^\bullet OH) \longrightarrow \text{dye decomposition} \qquad (1.7)$$

The nature of the pollutant species present in the reaction system plays a crucial role in determining the dominant photocatalytic degradation pathway. Cationic organic dyes, such as methylene blue (MB) (Houas et al., 2001; Jing, Wang, Zhang, Wang and Li, 2014; Vasiljevic et al., 2020) and Rhodamine B (RhB) (Vijaya Sankar and Ashok, 2020), are generally degraded predominantly through reduction processes, in which photogenerated electrons participate in the reduction of the positively charged dye molecules. In contrast, anionic dyes, such as methyl orange (MO) (Cerrato, Gaggero, Calza and Paganini, 2022), are more commonly degraded via oxidation pathways, where photogenerated holes or hydroxyl radicals act as the primary oxidizing agents.

One of the major challenges in photocatalysis is the recombination of photogenerated electron–hole pairs, as described in Equation (1.8). When recombination occurs prior to charge carrier participation in surface redox reactions, the absorbed photon energy is dissipated as heat or light, resulting in a significant loss of photocatalytic efficiency. Therefore, suppressing charge carrier recombination and promoting efficient charge separation are critical objectives in the design and optimization of high-performance photocatalysts.

$$h^+ + e^- \longrightarrow \text{recombination} + \text{energy (heat or photons)} \quad (1.8)$$

1.3 Photocatalyst

The core component of the photocatalytic process is the photocatalyst material, which is most commonly a semiconductor. Semiconductor materials are employed because of their ability to absorb light energy and generate photogenerated electron–hole pairs that drive subsequent redox reactions. Widely studied photocatalysts include titanium dioxide (TiO_2), zinc oxide (ZnO), and a variety of metal oxides and sulfides, owing to their suitable electronic structures, chemical stability, and relatively low cost (Fujishima et al., 1972; Hoffmann et al., 1995; Linsebigler et al., 1995).

In semiconductor photocatalysts, the absorption of photons promotes electrons from the valence band to the conduction band when the photon energy is equal to or greater than the band gap energy of the material. Consequently, the magnitude of the band gap determines the range of light wavelengths that can be absorbed and utilized for photocatalytic reactions. Many conventional photocatalysts, such as TiO_2 and ZnO, possess wide band gaps and are therefore primarily active under ultraviolet (UV) irradiation, which represents only a small fraction of the solar spectrum (Chen et al., 2007).

To enhance photocatalytic efficiency and extend light absorption into the visible region, various modification strategies have been widely adopted. These strategies include surface modification, elemental doping, coupling with co-catalysts, and the construction of nanostructured materials. Doping with metal or non-metal

elements is often employed to tailor the electronic structure and reduce the band gap energy, thereby improving visible-light absorption and charge carrier separation (Asahi, Morikawa, Ohwaki, Aoki and Taga, 2001; Kudo et al., 1988). The introduction of co-catalysts can further enhance surface reaction kinetics by providing additional active sites and facilitating charge transfer. In addition, the fabrication of nanostructured photocatalysts can increase the specific surface area and shorten charge carrier diffusion distances, which helps suppress electron–hole recombination and improve overall photocatalytic performance (Schneider et al., 2014).

1.4 Perovskite material

Perovskite materials have attracted significant attention in the fields of materials science, physics, and photovoltaics due to their remarkable physicochemical properties and broad potential for energy and environmental applications. These materials are defined by a characteristic crystal structure known as the perovskite structure, which is typically described by the general chemical formula ABX_3. In this structure, the B-site cation is located at the center of an octahedron formed by X-site anions, while the A-site cation occupies the interstitial spaces between the octahedra. The A-site is commonly occupied by alkaline earth metals or lanthanides, the B-site by transition metals, and the X-site by an anion, most frequently oxygen (Irshad et al., 2022). A schematic illustration of the perovskite crystal structure is shown in Figure 1.2.

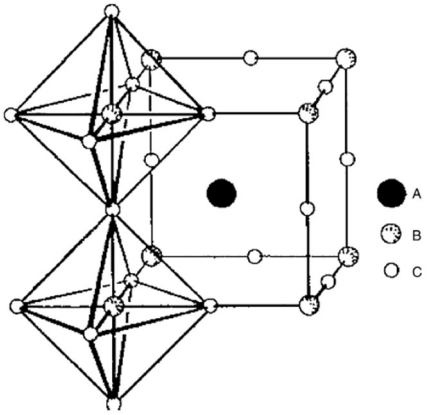


Figure 1.2 Perovskite structure illustrated for ABO_3 (Li, Soh and Wu, 2004).

In recent years, perovskite materials have also been increasingly explored in the field of photocatalysis due to their unique and tunable properties. These materials have been demonstrated to possess adjustable band gap energies, strong light absorption capabilities, and favorable charge carrier transport characteristics, which are critical factors for efficient photocatalytic performance (Kudo and Miseki, 2009). Similar to conventional semiconductor photocatalysts, perovskite materials can absorb photons to generate electron–hole pairs that subsequently participate in surface redox reactions.

One of the most attractive features of perovskite materials is the high degree of compositional flexibility offered by the ABX_3 structure. By substituting different elements at the A, B, and X sites, the electronic structure and band gap energy of perovskite materials can be systematically tuned. This tunability enables the design of perovskite photocatalysts with absorption edges that match specific regions of the solar spectrum, thereby enhancing visible-light-driven photocatalytic activity. In addition, many perovskite materials exhibit strong absorption in the visible and near-infrared regions, allowing efficient utilization of a broad range of solar wavelengths. The relatively high charge carrier mobility reported in many perovskite systems further contributes to improved charge separation and reduced recombination losses during photocatalytic reactions (Snaith, 2013).

Despite these advantages, the practical application of perovskite materials in photocatalysis remains challenged by their limited stability under operational conditions. Many perovskite materials are sensitive to moisture, thermal stress, and prolonged light irradiation, which can lead to structural degradation and performance loss. As a result, considerable research efforts have been directed toward improving the chemical and structural stability of perovskite photocatalysts through compositional engineering, surface modification, and the development of protective architectures (Li et al., 2016; Niu, Guo and Wang, 2015; Zhou et al., 2020).

Although perovskite-based photocatalysis is still a relatively emerging research area, it has demonstrated significant promise as an environmentally friendly and efficient approach for addressing energy conversion and environmental remediation challenges. Ongoing research is focused on optimizing perovskite compositions,

enhancing long-term stability, and improving scalability to facilitate their practical deployment in real-world photocatalytic applications.

1.5 Sol-Gel method

The sol-gel method is a versatile and widely used chemical process for the synthesis of various materials, including nanomaterials and catalysts. It is a technique that involves the transformation of a solution (sol) into a gel-like or solid material (gel) through controlled chemical reactions. The sol-gel process can be used to create a wide range of materials with diverse properties and applications (Vasiljevic et al., 2020; Vijaya Sankar et al., 2020; Wu et al., 2012).

1.5.1 The basic steps in the Sol-Gel process

1. The process begins with the preparation of a solution, often containing metal alkoxides, metal chlorides, or other precursor compounds. This solution, known as a sol, typically consists of metal ions or molecules dispersed in a solvent.

2. The sol undergoes a chemical reaction, typically hydrolysis and condensation reactions, which result in the formation of a three-dimensional network of interconnected particles or polymers. This network transforms the liquid sol into a gel, which is a semi-solid or solid-like material.

3. After gelation, the material is allowed to age or mature for a period of time, during which further chemical reactions and structural changes can occur. Following aging, the gel is carefully dried to remove the solvent, leaving behind a solid material.

4. Depending on the desired properties and applications of the material, heat treatment (calcination) may be performed at elevated temperatures. This step can help to enhance the crystallinity and stability of the final product.

1.5.2 The key advantages of the Sol-Gel method

1. The sol-gel process allows for precise control over the composition and uniform distribution of components in the material.

2. It can be used to produce a wide range of materials with different compositions and properties.

3. The sol-gel method often yields highly pure materials with low levels of impurities.

4. The structure and properties of the final material can be controlled by adjusting parameters such as precursor composition, solvent, pH, and processing conditions.

5. The sol-gel process can be used to create nanomaterials and nanocomposites with unique properties.

1.6 Doping photocatalyst

Doping in photocatalysts refers to the deliberate incorporation of foreign atoms, ions, or molecules (dopants) into the crystal lattice of a photocatalytic material. This strategy is widely employed to tailor the structural, electronic, and surface properties of photocatalysts in order to enhance their performance in light-driven chemical reactions. Through controlled doping, the intrinsic limitations of pristine photocatalysts, such as wide band gap energy and rapid charge carrier recombination, can be effectively mitigated. One of the primary objectives of doping is the modification of the band gap energy of the photocatalyst. By introducing suitable dopant species, the electronic structure of the host material can be altered, allowing light absorption to be extended into the visible region of the solar spectrum, which constitutes the majority of solar irradiation. As a result, the photocatalyst becomes more efficient in harvesting solar energy and generating photogenerated charge carriers under visible-light illumination (Asahi et al., 2001; Di Valentin, Pacchioni and Selloni, 2005).

In addition to band gap engineering, doping can significantly influence charge carrier dynamics. Dopant atoms can introduce localized energy levels within the band gap or induce lattice distortions, which can act as electron or hole trapping sites. These features promote the separation and migration of photogenerated electron–hole pairs while suppressing their recombination, which is a major loss pathway in photocatalytic systems. Consequently, enhanced charge carrier lifetime and mobility can be achieved, leading to improved photocatalytic activity. Furthermore, doping can modify the surface chemistry of photocatalysts by introducing new active sites or altering surface adsorption characteristics. Such changes can improve the interaction between the photocatalyst surface and reactant molecules, thereby enhancing reaction selectivity

and catalytic efficiency for specific photocatalytic processes, including pollutant degradation and redox reactions (Chong et al., 2010).

Doping with rare earth metal ions has been extensively investigated as an effective approach to enhance the photocatalytic performance of perovskite-based materials. Rare earth elements, such as cerium (Ce), lanthanum (La), and europium (Eu), are known to possess unique electronic configurations with partially filled 4f orbitals, which can impart distinctive optical, electronic, and catalytic properties to perovskite photocatalysts. In particular, the coexistence of multiple oxidation states (e.g., Ce^{3+}/Ce^{4+}) can facilitate efficient charge transfer and act as redox centers, thereby further improving photocatalytic efficiency (Wendari et al., 2021).

1.7 References

Asahi, R., Morikawa, T., Ohwaki, T., Aoki, K., & Taga, Y. (2001). Visible-light photocatalysis in nitrogen-doped titanium oxides. *science*. *293*(5528), 269-271.

Brundtland, G. H. (1987). Our common future world commission on environment and developement.

Canton, H. (2021) United nations environment programme—unep. The Europa directory of international organizations 2021. Routledge. p. 188-214.

Cerrato, E., Gaggero, E., Calza, P., & Paganini, M. C. (2022). The role of Cerium, Europium and Erbium doped TiO2 photocatalysts in water treatment: A mini-review. *Chemical Engineering Journal Advances*. *10*(100268). doi:10.1016/j.ceja.2022.100268.

Chen, X., & Mao, S. S. (2007). Titanium dioxide nanomaterials: synthesis, properties, modifications, and applications. *Chemical Reviews*. *107*(7), 2891-2959.

Chen, X., Shen, S., Guo, L., & Mao, S. S. (2010). Semiconductor-based photocatalytic hydrogen generation. *Chemical Reviews*. *110*(11), 6503-6570.

Chong, M. N., Jin, B., Chow, C. W., & Saint, C. (2010). Recent developments in photocatalytic water treatment technology: a review. *Water research*. *44*(10), 2997-3027.

Di Valentin, C., Pacchioni, G., & Selloni, A. (2005). Theory of carbon doping of titanium dioxide. *Chemistry of Materials*. *17*(26), 6656-6665.

Dockery, D. W., & Pope, C. A. (1994). Acute respiratory effects of particulate air pollution.

Fujishima, A., & Honda, K. (1972). Electrochemical photolysis of water at a semiconductor electrode. *nature*. *238*(5358), 37-38.

Hisatomi, T., Kubota, J., & Domen, K. (2014). Recent advances in semiconductors for photocatalytic and photoelectrochemical water splitting. *Chemical Society Reviews*. *43*(22), 7520-7535.

Hoffmann, M. R., Martin, S. T., Choi, W., & Bahnemann, D. W. (1995). Environmental applications of semiconductor photocatalysis. *Chemical Reviews*. *95*(1), 69-96.

Houas, A., Lachheb, H., Ksibi, M., Elaloui, E., Guillard, C., & Herrmann, J.-M. (2001). Photocatalytic degradation pathway of methylene blue in water. *Applied Catalysis B: Environmental*. *31*(2), 145-157. doi:10.1016/S0926-3373(00)00276-9.

Irshad, M., Ain, Q. t., Zaman, M., Aslam, M. Z., Kousar, N., Asim, M., . . . Imran, M. (2022). Photocatalysis and perovskite oxide-based materials: a remedy for a clean and sustainable future. *RSC Advances*. *12*(12), 7009-7039. doi:10.1039/D1RA08185C.

Jing, H.-P., Wang, C.-C., Zhang, Y.-W., Wang, P., & Li, R. (2014). Photocatalytic degradation of methylene blue in ZIF-8. *RSC Advances*. *4*(97), 54454-54462. doi:10.1039/C4RA08820D.

Kong, J., Yang, T., Rui, Z., & Ji, H. (2019). Perovskite-based photocatalysts for organic contaminants removal: Current status and future perspectives. *Catalysis Today*. *327*(47-63. doi:10.1016/j.cattod.2018.06.045.

Kudo, A., & Miseki, Y. (2009). Heterogeneous photocatalyst materials for water splitting. *Chemical Society Reviews*. *38*(1), 253-278.

Kudo, A., Tanaka, A., Domen, K., Maruya, K.-i., Aika, K.-i., & Onishi, T. (1988). Photocatalytic decomposition of water over NiO2 K4Nb6O17 catalyst. *Journal of Catalysis*. *111*(1), 67-76.

Lewis, N. S., & Nocera, D. G. (2006). Powering the planet: Chemical challenges in solar energy utilization. *Proceedings of the National Academy of Sciences*. *103*(43), 15729-15735.

Li, C., Soh, K. C. K., & Wu, P. (2004). Formability of ABO3 perovskites. *Journal of Alloys and Compounds*. *372*(1), 40-48. doi:10.1016/j.jallcom.2003.10.017.

Li, W., Zhang, W., Van Reenen, S., Sutton, R. J., Fan, J., Haghighirad, A. A., . . . Snaith, H. J. (2016). Enhanced UV-light stability of planar heterojunction perovskite solar cells with caesium bromide interface modification. *Energy & Environmental Science*. *9*(2), 490-498.

Linsebigler, A. L., Lu, G., & Yates Jr, J. T. (1995). Photocatalysis on TiO2 surfaces: principles, mechanisms, and selected results. *Chemical Reviews*. *95*(3), 735-758.

Niu, G., Guo, X., & Wang, L. (2015). Review of recent progress in chemical stability of perovskite solar cells. *Journal of Materials Chemistry A*. *3*(17), 8970-8980.

Organization, W. H. (2020). World health statistics 2020.

Organization, W. H. (2023) Burden of disease attributable to unsafe drinking-water, sanitation and hygiene, 2019 update. World Health Organization.

Schneider, J., Matsuoka, M., Takeuchi, M., Zhang, J., Horiuchi, Y., Anpo, M., & Bahnemann, D. W. (2014). Understanding TiO2 photocatalysis: mechanisms and materials. *Chemical Reviews*. *114*(19), 9919-9986.

Schwarzenbach, R. P., Egli, T., Hofstetter, T. B., Von Gunten, U., & Wehrli, B. (2010). Global water pollution and human health. *Annual review of environment and resources*. *35*(109-136).

Snaith, H. J. (2013). Perovskites: the emergence of a new era for low-cost, high-efficiency solar cells. *The journal of physical chemistry letters*. *4*(21), 3623-3630.

Vasiljevic, Z. Z., Dojcinovic, M. P., Vujancevic, J. D., Jankovic-Castvan, I., Ognjanovic, M., Tadic, N. B., . . . Nikolic, M. V. (2020). Photocatalytic degradation of methylene blue under natural sunlight using iron titanate nanoparticles prepared by a modified sol–gel method. *Royal Society Open Science*. *7*(9). doi:10.1098/rsos.200708.

Vijaya Sankar, K., & Ashok, M. (2020). Effect of preparation method on structural, morphological, optical properties and photocatalytic activities of visible light active semiconductor PbBi2Nb2O9 for various organic pollutant dyes. *Materials Science in Semiconductor Processing*. *106*(104773). doi:10.1016/j.mssp.2019.104773.

Wang, Q., & Domen, K. (2019). Particulate photocatalysts for light-driven water splitting: mechanisms, challenges, and design strategies. *Chemical Reviews*. *120*(2), 919-985.

Wendari, T. P., Arief, S., Mufti, N., Insani, A., Baas, J., Blake, G. R., & Zulhadjri. (2021). Structure-property relationships in the lanthanide-substituted PbBi2Nb2O9 Aurivillius phase synthesized by the molten salt method. *Journal of Alloys and Compounds*. *860*(158440). doi:10.1016/j.jallcom.2020.158440.

Wu, W., Liu, G., Liang, S., Chen, Y., Shen, L., Zheng, H., . . . Wu, L. (2012). Efficient visible-light-induced photocatalytic reduction of 4-nitroaniline to p-phenylenediamine over nanocrystalline PbBi2Nb2O9. *Journal of Catalysis*. *290*(13-17). doi:10.1016/j.jcat.2012.02.005.

Zhang, L., & Zhu, Y. (2012). A review of controllable synthesis and enhancement of performances of bismuth tungstate visible-light-driven photocatalysts. *Catalysis Science & Technology*. *2*(4), 694-706.

Zhou, W., Yang, L., Liu, L., Chen, Z., Zhou, A., Zhang, Y., . . . Zhao, Z. (2020). Synthesis of novel NiMo catalysts supported on highly ordered TiO2-Al2O3 composites and their superior catalytic performance for 4,6-dimethyldibenzothiophene hydrodesulfurization. *Applied Catalysis B: Environment and Energy*. *268*(118428).

Zou, Z., Ye, J., Sayama, K., & Arakawa, H. (2001). Direct splitting of water under visible light irradiation with an oxide semiconductor photocatalyst. *nature*. *414*(6864), 625-627.

CHAPTER II

LITERATURE REVIEWS

2.1 $Pb_2Nb_2O_9$ photocatalyst

$PbBi_2Nb_2O_9$ (Lead Bismuth Niobium Oxide) has a crystal structure that is related to the perovskite structure, belongs to the bismuth oxides family with a structure consisting of perovskite layers ($A_{m-1}B_mO_{3m+1}$) between bismuth oxide layers (Bi_2O_2) (Bi, Wu, Li, Wang and Fu, 2008). In this compound, lead (Pb) occupies the A-site, while bismuth (Bi) and niobium (Nb) occupy the B-site as shown in the Figure 2.1. $PbBi_2Nb_2O_9$ is a compound that has been investigated for various applications, including its potential use as a photocatalyst. Its specific properties and potential as a photocatalyst may depend on factors such as its composition and the synthesis method used.

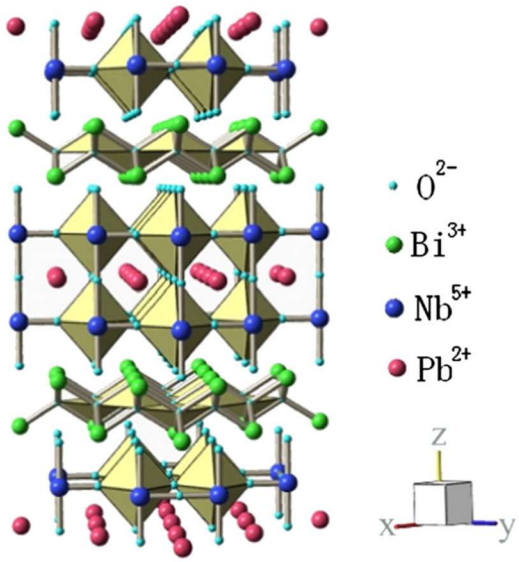


Figure 2.1 Schematic structure of $PbBi_2Nb_2O_9$ (Bi et al., 2008).

$PbBi_2Nb_2O_9$ (PBNO) has a double perovskite structure, which is characterized by its unique crystal arrangement. Double perovskites are a class of materials that have two different cations occupying the B-site of the perovskite structure, rather than a single cation as in the standard perovskite structure. This arrangement results in a crystal structure

that is distinct from the simple perovskite structure, and it can lead to unique properties and behaviors in the material. Double perovskites like $PbBi_2Nb_2O_9$ have been of interest for their potential in various applications, including photocatalysts.

The synthesis method plays a crucial role in determining the specific properties and characteristics of materials like $PbBi_2Nb_2O_9$. Different synthesis methods can yield materials with varying structures, compositions, and properties. In solid-State Reaction (SSR) method (Vijaya Sankar and Ashok, 2020), reactants are mixed in a solid state and heated to initiate chemical reactions that lead to the formation of the desired compound. This method can produce well-crystallized materials but may require high temperatures and long reaction times. Hydrothermal synthesis (HT) (Xie, Chang, Yang, Jiang and Zhao, 2016) involves the use of high-temperature and high-pressure aqueous solutions to promote chemical reactions. This method is known for producing finely crystalline and high-surface-area materials. It can result in materials with different morphologies and surface properties compared to SSR. In molten salt synthesis (MS) (Wendari et al., 2021), reactants are melted in a high-temperature salt medium. This method can lead to materials with unique properties and structures. It is particularly useful for compounds with high melting points. Sol-gel methods (SG) (Wu et al., 2012) involve the formation of a sol (a suspension of nanoscale particles in a liquid) and subsequent gelation to form a solid material. Modified sol-gel methods are variations of the traditional sol-gel process and are often used to tailor the properties of materials, including PBNO, by incorporating dopants or altering reaction conditions.

The study by Wu reports the successful preparation of nanocrystalline PBNO using a modified sol-gel method and its application as a photocatalyst for the reduction of 4-nitroaniline (4-NA) to p-phenylenediamine (PPD). The reduction process achieved a remarkable 99% selectivity and was conducted under visible light irradiation for 150 minutes in a nitrogen (N_2) atmosphere (Wu et al., 2012). The reaction mechanism involved the use of $C_2O_4^{2-}$ ions as hole scavengers. In photocatalytic processes, electrons and holes are generated. Hole scavengers help prevent the recombination of electrons and holes, enhancing the efficiency of the photocatalytic reaction. A mechanism for the photocatalytic reduction of 4-NA to PPD in Figure 2.2.

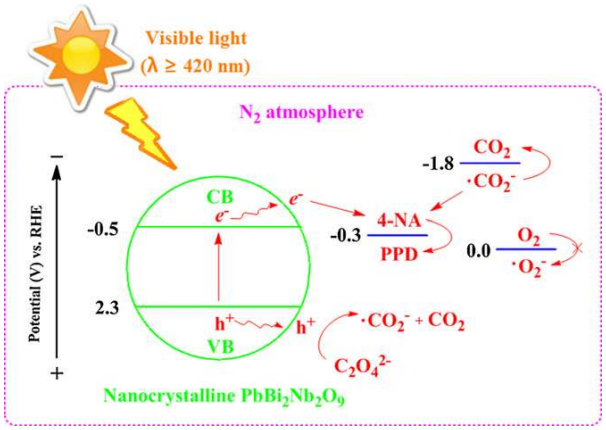


Figure 2.2 Mechanism for the photocatalytic reduction of 4-NA to PPD by nanocrystalline $PbBi_2Nb_2O_9$ (Wu et al., 2012).

The study by Sankar and Ashok (Vijaya Sankar et al., 2020) compares the effects of two different preparation methods, solid-state reaction (SSR) and sol-gel (SG), on the properties and performance of PBNO. The study found that PBNO-SG, synthesized via the sol-gel method, exhibited smaller crystalline size and a higher surface area compared to PBNO-SSR, synthesized through solid-state reaction. Smaller crystalline size can lead to more exposed surface area, which is often beneficial for catalytic applications. This provides a larger number of active sites for chemical reactions. PBNO-SG had lower photoluminescence intensity compared to PBNO-SSR. This suggests that PBNO-SG exhibited a lower recombination rate of electron-hole pairs. In photocatalysis, a lower recombination rate is desirable because it means that more charge carriers (electrons and holes) are available for chemical reactions, resulting in more efficient photocatalysis. PBNO-SG was found to be more suitable for degrading organic pollutants under visible light compared to PBNO-SSR.

2.2 Modified $Pb_2Nb_2O_9$ photocatalysts

Modifying the structure and properties of $PbBi_2Nb_2O_9$ through cation substitution is a common strategy researcher to tailor materials to meet specific performance requirements. The choice of the cation and the extent of substitution play crucial roles in determining the final properties of the modified material. These

modifications can have a significant impact on the performance of material in photocatalytic applications. Examples of cation substitutions include W^{6+} (Kim, Borse, Jang, Jeong and Lee, 2008), La^{3+}, Nd^{3+} (Wendari et al., 2021) and Fe^{3+} (Gu, Kim, Kim and Lim, 2023). Each of these cations has unique properties and ionic radii, which can result in various changes to the structure of material and behavior.

The partial substitution of niobium ions (Nb^{5+}) with tungsten ions (W^{6+}) in the PBNO crystal structure was reported by Kim et al. (Kim et al., 2008). It is mentioned that when the tungsten doping in $PbBi_2Nb_{2-x}W_xO_9$ exceeds x=0.15, the particles lose their uniformity and more phase impurities appear. This suggests that there may be a limit to the amount of tungsten that can be effectively substituted into the crystal structure without adversely affecting the material's uniformity. Despite the potential limitations in terms of uniformity and phase impurities, the W-doped PBNO material is reported to exhibit high photodecomposition activity.

Fe-doped $PbBi_2Nb_2O_9$ (Gu et al., 2023), denoted as PBFNO, was synthesized through a solid-state reaction method. Iron (Fe) was used as a dopant, and it was incorporated into the crystal structure by substituting Bi ions. The XRD pattern (Figure 2.3) revealed significant changes in the structure of material after Fe doping. The highest peak shifted, and the peaks broadened. This is attributed to a small decrease in the lattice distance, which is a result of substituting the larger ionic radius of Bi^{3+} (0.96 Å) with the smaller ionic radius of Fe^{3+} (0.64 Å). This structural change can have a profound impact on the material properties.

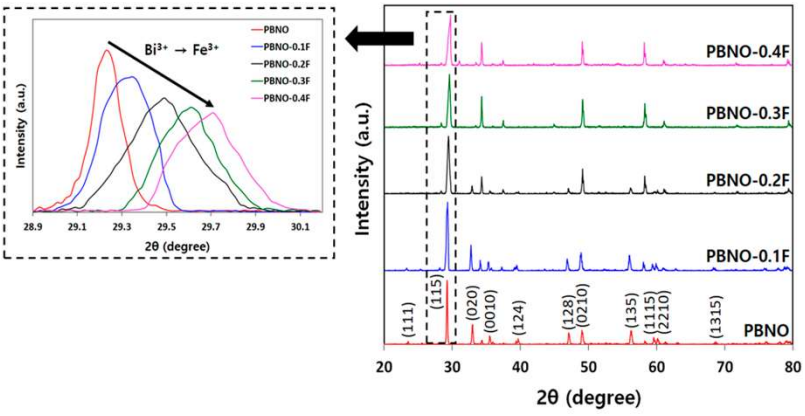


Figure 2.3 XRD patterns of as-prepared PBNO and PBFNO samples by solid-state reaction.

The band gap energy of PBFNO was found to decrease compared to the pristine PBNO. This suggests that PBFNO is better suited for absorbing and utilizing visible light energy for photocatalytic reactions. The presence of Fe dopants in PBFNO is reported to have a dual role. Firstly, they form intermediate bands, which can facilitate absorption of photons at specific energies. Secondly, they serve as electron-hole traps, which reduce the recombination of charge carriers. The reduction in photoluminescence intensity after Fe doping suggests that fewer charge carriers are recombining, enhancing the material's charge separation efficiency. Interestingly, the statement also mentions that the excess Fe dopants act as recombination centers. These are locations where electrons and holes recombine, potentially reducing charge separation efficiency. However, despite this, PBFNO demonstrates superior photocatalytic activity for the degradation of methylene blue, particularly under visible light irradiation at pH 12.

2.3 Modified photocatalyst by Ce-doping

Cerium is indeed an interesting element among the lanthanides due to its unique properties, including its band gap, optical properties, and catalytic potential. A smaller band gap, indicates that cerium can efficiently absorb light in the visible region, making it a good candidate for various optical applications. Absolutely, the ability of cerium to transition between Ce^{3+} and Ce^{4+} oxidation states enhance its catalytic potential (Ellappan and Miranda, 2014).

The cerium is doped into titanium dioxide (Chen et al., 2010) (Liu, Li, Leng and Li, 2003), it results in a shift towards the visible region in terms of its optical properties. This shift towards the visible region can make the material more effective in capturing and utilizing visible light, which has important implications for applications such as photocatalysis and solar energy conversion.

The role of Ce-doped TiO_2 in photocatalysis (Cerrato, Gaggero, Calza and Paganini, 2022). Ce ions can exist in two oxidation states, Ce^{3+} and Ce^{4+}. The presence of these ions can serve as electron traps, which means they can capture and store electrons, reducing the recombination of electrons and holes. This is a critical factor in enhancing the efficiency of photocatalytic reactions. Ce-doping can also extend the

absorption range of TiO_2 into the visible light spectrum. Moreover, the introduction of Ce ions into TiO_2 can create additional catalytic active sites on the surface of the photocatalyst. These active sites facilitate the interaction between the photocatalyst and the target molecules in the photodegradation reaction, such as organic pollutants like methyl orange. The mechanism of methyl orange degradation as shown in Figure 2.4.

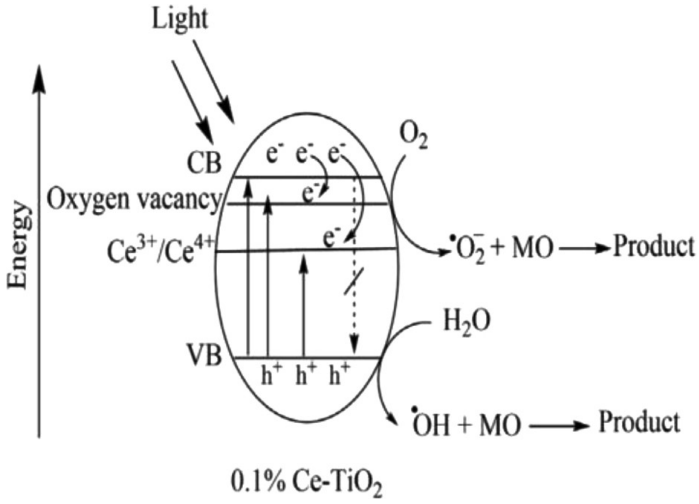


Figure 2.4 The mechanism of methyl orange dye degradation over 0.1% Ce-doped TiO_2 under UV light irradiation.

Photocatalytic hydrogen evaluation study the behavior of hybrid $Ce^{4+/3+}$ doped into perovskite magnesium zirconate nano cubes ($MgZrO_3$ NCs) (Prashanth et al., 2021) to methyl orange degradation. The band edge positions in pristine ZrO_2 and $MgZrO_3$ are shown in the Figure 2.5, Incorporation of Ce dopant to $MgZrO_3$ modified the band edge positions of $Ce^{4+/3+}$: $MgZrO_3$ NCs. The shift in band edge positions indicated that the introduction of Ce dopants led to an increase in the generation of electron-hole pairs upon exposure to light. The rearrangement of band edge positions and the greater electro positivity of zirconia in $Ce^{4+/3+}$: $MgZrO_3$ NCs played a role in suppressing the recombination of photo-generated electrons and holes.

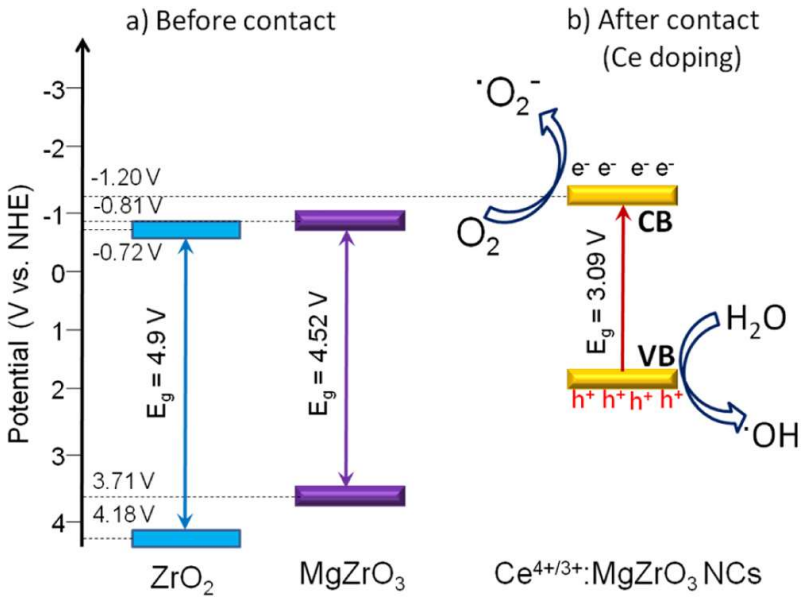


Figure 2.5 Band edge positions of (a) Pristine ZrO_2 and $MgZrO_3$ (b) Band alignment in case of $Ce^{4+/3+}$: $MgZrO_3$ NCs.

As a result of the modified band edge positions and the suppression of recombination, the $Ce^{4+/3+}$: $MgZrO_3$ NCs, containing 9 mol% of Ce dopant, exhibited a significantly higher photocatalytic activity. They achieved a photocatalytic hydrogen production rate of 13,318 μmol $h^{-1}g^{-1}$, which was 6.2 times greater than pristine ZrO_2 and 4.1 times greater than $MgZrO_3$. This suggests that the introduction of Ce dopants enhanced the efficiency of hydrogen generation. In addition, methyl orange degradation efficiency of $Ce^{4+/3+}$: $MgZrO_3$ NCs reached 93% within 120 minutes. This high efficiency can be attributed to the presence of abundant photo-active centers and defects within the material, which again helps in suppressing charge carrier recombination and promotes efficient dye degradation.

The study by Cao investigates the use of Ce-doped $BiFeO_3$ (BCFO) as a photocatalyst to enhance the photo-Fenton degradation of tetracycline (TC). In the photo-Fenton system, the researchers utilize a combination of ferrous ions (Fe^{2+}) and hydrogen peroxide (H_2O_2) activated by light to generate hydroxyl radicals ($^{\bullet}OH$) (Cao et al., 2024). A previous study by Lu revealed that pure $BiFeO_3$ (BFO) had a high electron-hole recombination rate. This recombination can reduce the efficiency of the photocatalytic process. Ce^{3+} ions, introduced into the BCFO structure, have the

capability to activate H_2O_2 and $^{\bullet}OH$, similar to Fe^{2+} (Lu et al., 2022). This makes Ce^{3+} ions valuable for enhancing the photo-Fenton reaction. Meanwhile, cerium is doped into the BFO structure as Ce^{4+}, which has a higher valence than the original Bi^{3+} ions. This Ce^{4+} can act as a donor ion within the oxygen octahedron, helping to maintain charge neutrality and suppress the formation of oxygen vacancies (OVs) in the material. The introduction of Ce ions into BFO narrows the band gap of the material. The photoluminescence intensity of BCFOs is lower than that of BFO, indicating a reduction in the electron-hole recombination rate. While Ce doping has beneficial effects on photocatalytic performance, the study found that when the Ce content was increased to 9%, excess Ce prevented H_2O_2 from decomposing effectively. It also precipitated out and formed cerium dioxide (CeO_2), which coated the active catalytic sites and acted as a recombination center for photogenerated carriers. As a result, the researchers found that 7% Ce doping provided the best photocatalytic performance. The photo-Fenton system using BCFO-7 as a photocatalyst achieved a high degradation rate of tetracycline (TC), reaching 97% at an initial pH of 3, and maintaining a degradation rate of 91% at pH 4. The mechanism for the degradation of TC by BCFO-7 is shown in the figure 2.6.

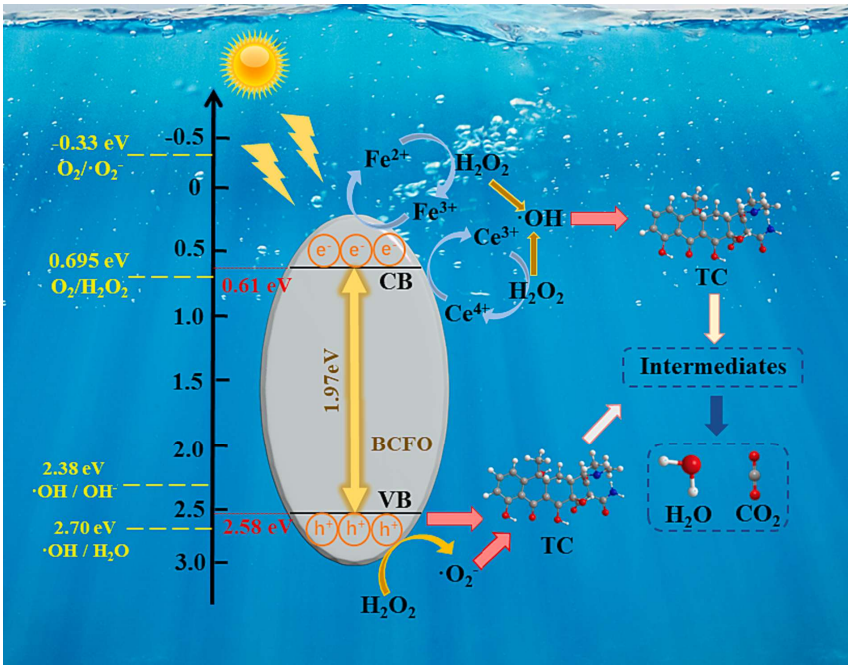


Figure 2.6 Mechanistic diagram of TC degradation by BCFO-7.

2.4 References

Bi, J., Wu, L., Li, Z., Wang, X., & Fu, X. (2008). A citrate complex process to prepare nanocrystalline PbBi2Nb2O9 at a low temperature. *Materials Letters*. *62*(1), 155-158. doi:10.1016/j.matlet.2007.04.115.

Cao, C., Lu, Z., Wang, L., Li, L., Deng, D., Liao, D., & Mo, C. (2024). Ce-doped BiFeO3 as a photocatalyst to enhance photo-Fenton degradation of tetracycline. *Journal of Photochemistry and Photobiology A: Chemistry*. *446*(115161). doi:10.1016/j.jphotochem.2023.115161.

Cerrato, E., Gaggero, E., Calza, P., & Paganini, M. C. (2022). The role of Cerium, Europium and Erbium doped TiO2 photocatalysts in water treatment: A mini-review. *Chemical Engineering Journal Advances*. *10*(100268). doi:10.1016/j.ceja.2022.100268.

Chen, S. W., Lee, J. M., Lu, K. T., Pao, C. W., Lee, J. F., Chan, T. S., & Chen, J. M. (2010). Band-gap narrowing of TiO2 doped with Ce probed with x-ray absorption spectroscopy. *Applied Physics Letters*. *97*(1). doi:10.1063/1.3460916.

Ellappan, P., & Miranda, L. R. (2014). Synthesis and Characterization of Cerium Doped Titanium Catalyst for the Degradation of Nitrobenzene Using Visible Light. *International Journal of Photoenergy*. *2014*(1), 756408. doi:10.1155/2014/756408.

Gu, Y., Kim, M., Kim, H. S., & Lim, D.-H. (2023). Synthesis and Characterization of Fe Doped Aurivillius-Phase PbBi2Nb2O9 Perovskite and Their Photocatalytic Activity on the Degradation of Methylene Blue. *Catalysts*. *13*(2), 399. doi:10.3390/catal13020399.

Kim, H. G., Borse, P. H., Jang, J. S., Jeong, E. D., & Lee, J. S. (2008). Enhanced photochemical properties of electron rich W-doped PbBi2Nb2O9 layered perovskite material under visible-light irradiation. *Materials Letters*. *62*(8), 1427-1430. doi:10.1016/j.matlet.2007.08.089.

Liu, H., Li, X. Z., Leng, Y. J., & Li, W. Z. (2003). An Alternative Approach to Ascertain the Rate-Determining Steps of TiO2 Photoelectrocatalytic Reaction by

Electrochemical Impedance Spectroscopy. *The Journal of Physical Chemistry B*. *107*(34), 8988-8996. doi:10.1021/jp034113r.

Lu, Z., Xie, T., Wang, L., Li, L., Cao, C., & Mo, C. (2022). Low content Ni-doped BiFeO3 with efficient photo-Fenton degradation of tetracycline. *Optical Materials*. *134*(113185). doi:10.1016/j.optmat.2022.113185.

Prashanth, K. S., Raghu, M. S., Alharthi, F. A., Sreenivasa, S., Anusuya Devi, V. S., Krishnaiah, P., . . . Parashuram, L. (2021). Solar light sensitive hybrid Ce4+/3+ doped perovskite magnesium zirconate nano cubes for photocatalytic hydrogen evolution and organic pollutant degradation in water. *Journal of Environmental Chemical Engineering*. *9*(4), 105364. doi:10.1016/j.jece.2021.105364.

Vijaya Sankar, K., & Ashok, M. (2020). Effect of preparation method on structural, morphological, optical properties and photocatalytic activities of visible light active semiconductor PbBi2Nb2O9 for various organic pollutant dyes. *Materials Science in Semiconductor Processing*. *106*(104773). doi:10.1016/j.mssp.2019.104773.

Wendari, T. P., Arief, S., Mufti, N., Insani, A., Baas, J., Blake, G. R., & Zulhadjri. (2021). Structure-property relationships in the lanthanide-substituted PbBi2Nb2O9 Aurivillius phase synthesized by the molten salt method. *Journal of Alloys and Compounds*. *860*(158440). doi:10.1016/j.jallcom.2020.158440.

Wu, W., Liu, G., Liang, S., Chen, Y., Shen, L., Zheng, H., . . . Wu, L. (2012). Efficient visible-light-induced photocatalytic reduction of 4-nitroaniline to p-phenylenediamine over nanocrystalline PbBi2Nb2O9. *Journal of Catalysis*. *290*(13-17). doi:10.1016/j.jcat.2012.02.005.

Xie, H., Chang, X., Yang, W., Jiang, Y., & Zhao, Y. (2016). Hydrothermal Synthesis and Photocatalytic Activities of PbBi2Nb2O9 Nanoplates. *Synthesis and Reactivity in Inorganic, Metal-Organic, and Nano-Metal Chemistry*. *46*(7), 1090-1094. doi:10.1080/15533174.2015.1004428.

CHAPTER III
EXPERIMENTAL SECTION

3.1 Materials and reagents

The following materials and reagents were used as starting materials: lead nitrate ($Pb(NO_3)_2$) (99%, KemAus), bismuth nitrate pentahydrate ($Bi(NO_3)_3•5H_2O$) (≥98%, CARLO ERBA Reagents), ammonium niobate oxalate hydrate ($C_4H_4NNbO_9•H_2O$) (99.99%, Aldrich), citric acid monohydrate ($C_6H_8O_7•H_2O$) (99.5%, CARLO ERBA Reagents), cerium nitrate hexahydrate ($Ce(NO_3)_3•6H_2O$) (99.5%, ACROS ORGANICS), ammonium solution (NH_4OH) (30%, CARLO ERBA Reagents), nitric acid (HNO_3) (69.5%, CARLO ERBA Reagents) and hydrogen peroxide (H_2O_2) (30%, CARLO ERBA Reagents).

3.2 Sample preparation

$PbBi_2Nb_2O_9$ (PBNO) was prepared by sol-gel method. Starting materials including $Pb(NO_3)_2$, $Bi(NO_3)_3•5H_2O$, $C_4H_4NNbO_9•H_2O$ and $C_6H_8O_7•H_2O$. The compounds are dissolved in a solution containing 30 mL of 30% H_2O_2 aqueous solution. The solution is stirred at 400 rpm for 5 minutes to ensure uniform mixing of the precursors. 2 mL of 6M HNO_3 is added to the mixture. The mixture is then heated at 65℃ for an hour. Then, the pH of the solution is adjusted to around 6.5 by slowly adding NH_4OH to obtain a yellow solution. This step must be careful control of pH to ensure the desired chemical reaction occur. The precursor solution undergoes a transformation, turning into a resin-like gel. The obtained gel is dried by heating at 120℃ for 24 hours. This step removes excess solvent and helps in the formation of a solid material. Then, the dried gel was preheated at 300℃ for 2 hours to remove organic compounds and calcined at different temperatures. In this work, it was calcined at 650℃, 700℃, 750℃ and 800℃ for 4 hours.

Synthesis Ce-doped of $PbBi_{2-x}Ce_xNb_2O_9$. The general synthesis steps are similarly as the PBNO preparation method. The main difference being the introduction $Ce(NO_3)_3•6H_2O$ as a dopant to replace some of the bismuth ions. The starting materials include $Pb(NO_3)_2$, $Bi(NO_3)_3•5H_2O$, $Ce(NO_3)_3•6H_2O$ (to provide cerium ions for doping), $C_4H_4NNbO_9•H_2O$ and $C_6H_8O_7•H_2O$. The cerium nitrate hexahydrate was calculated in a ratio corresponding to the desired Ce doping level, x= 0.02, 0.05, 0.08, 0.2, 0.5 and 0.8 respectively.

3.3 Characterizations

3.3.1 X-ray diffraction (XRD) and structure refinement

X-ray diffraction (XRD) was employed to analyze the structural characteristics of the synthesized materials. This technique was used to obtain detailed information regarding the crystal structure, phase composition, and crystallinity of the samples. Prior to measurement, the obtained powders were finely ground and carefully packed into a standard sample holder to ensure a flat and homogeneous surface.

The XRD patterns were recorded using a Bruker D2 Phaser diffractometer equipped with Cu Kα radiation (λ = 1.5406 Å). Data collection was carried out over a 2θ range of 10° to 70°, with a step size of 0.02° and a scan speed of 0.2 s per step. These measurement conditions were selected to achieve sufficient resolution for phase identification and structural analysis.

The recorded diffraction patterns were subsequently analyzed and compared with standard reference data obtained from the Physical Sciences Data-Science (PSDS) database to identify crystalline phases and evaluate phase purity. Structural refinement and detailed analysis were conducted based on the indexed diffraction peaks to assess any structural changes induced by compositional modification.

3.3.2 Scanning electron microscopy (SEM) and Energy dispersive X-ray spectroscopy (EDX).

Scanning electron microscopy (SEM) was employed to examine the surface morphology, particle distribution, and particle size of the synthesized materials at the

microscale. SEM observations were carried out using a JEOL JSM-6010LV scanning electron microscope. The measurements were conducted under an accelerating voltage of 20 kV with a working distance of 9.9 mm, which provided sufficient resolution and contrast for morphological analysis.

Energy-dispersive X-ray spectroscopy (EDS) was used in conjunction with SEM to perform qualitative and quantitative elemental composition analysis of the samples. The EDS measurements were conducted using an Oxford Instruments X-Max detector with an active area of 50 mm^2, enabling elemental mapping and area analysis. This technique was applied to confirm the presence and distribution of constituent elements in the samples and to verify the successful incorporation of dopant elements within the photocatalyst structure.

3.3.3 X-ray photoelectron spectroscopy (XPS).

X-ray photoelectron spectroscopy (XPS) was employed to investigate the surface chemical composition and electronic states of the constituent elements in the synthesized materials. The measurements were carried out at the Thailand Center of Excellence in Physics (ThEP), Chiang Mai University.

XPS spectra of all samples were collected using an AXIS Ultra DLD X-ray photoelectron spectrometer (Kratos Analytical Ltd., Manchester, England) equipped with a monochromatized Al K_α X-ray source (photon energy = 1486.6 eV). During data analysis, the binding energy scale was calibrated by referencing the C 1s peak at 284.8 eV, which originates from adventitious carbon on the sample surface. This calibration ensured accurate determination of the binding energies and reliable comparison of chemical states among the samples.

3.3.4 UV-Visible spectrophotometer.

UV–Visible diffuse reflectance spectroscopy (DRS) was employed to investigate the optical properties of the synthesized materials. The measurements were carried out using an Agilent UV–Vis–NIR spectrophotometer (Cary 60 UV–Vis) operating in double-beam mode. The diffuse reflectance spectra (%R) were recorded over a

wavelength range of 200–800 nm, which covers both the ultraviolet and visible regions of the electromagnetic spectrum.

The obtained reflectance data were analyzed using the Kubelka–Munk function, which is commonly applied to convert diffuse reflectance measurements into an equivalent absorption coefficient. The Kubelka–Munk function is expressed as:

$$F(R) = \frac{(1-R)^2}{2R} \tag{3.1}$$

where R represents the measured reflectance, defined as the ratio of the reflectance of the sample to that of the reference standard ($\%R_{sample}/\%R_{standard}$).

The optical band gap energy (E_g) of the samples was determined by extrapolating the linear region of the Tauc plot, constructed by plotting $(F(R)h\nu)^{1/2}$ as a function of the photon energy ($h\nu$). This method is based on the assumption of an indirect allowed electronic transition and provides an estimation of the band gap energy from the intersection of the extrapolated linear portion with the photon energy axis.

3.3.5 Photoluminescence (PL).

Photoluminescence (PL) spectroscopy was employed to investigate the optical emission properties and charge carrier recombination behavior of the synthesized materials. PL is a phenomenon in which photons are emitted from a material following the absorption of higher-energy photons. This process occurs when electrons are excited from lower energy states to higher energy states upon photon absorption and subsequently relax back to lower energy states, accompanied by photon emission. The emitted photons typically possess lower energy (longer wavelength) than the absorbed photons due to non-radiative energy losses within the material.

Prior to measurement, the obtained powder samples were carefully packed into a suitable sample holder and placed into the measurement chamber. The PL spectra were recorded using a HORIBA Scientific Fluoro Max-Plus spectrofluorometer with an excitation wavelength (λ_{ex}) of 315 nm. The recorded PL spectra were used to evaluate the recombination efficiency of photogenerated electron–hole pairs, where

lower PL intensity generally indicates suppressed radiative recombination and improved charge carrier separation in the photocatalyst.

3.3.6 X-ray adsorption spectroscopy (XAS)

X-ray absorption spectroscopy (XAS) was employed as a powerful analytical technique to investigate the electronic and local structural properties of the synthesized materials. This technique is based on the interaction between incident X-rays and matter and is widely used in chemistry, physics, materials science, and biology for probing the local atomic environment. XAS is particularly suitable for studying complex materials such as nanoparticles, semiconductors, and superconductors, as it provides element-specific information independent of long-range crystallinity.

A typical XAS spectrum can be divided into two main regions: the X-ray Absorption Near-Edge Structure (XANES) and the Extended X-ray Absorption Fine Structure (EXAFS), as illustrated in Figure 3.1. The XANES region, located near the absorption edge, provides information related to the oxidation state, coordination geometry, and electronic structure of the absorbing atom. In contrast, the EXAFS region, which extends beyond the absorption edge, yields quantitative information on the local atomic structure, including interatomic distances, coordination numbers, and structural disorder around the absorbing atom.

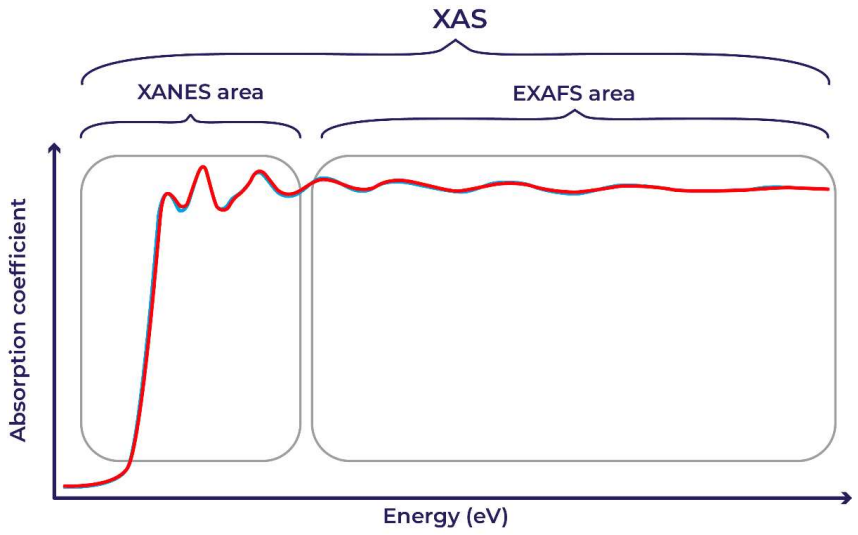


Figure 3.1 XANES and EXAFS region within XAS (Kartashov, Chernov, Polyanichenko and Butakova, 2021).

XAS measurements were conducted at two beamlines of the Synchrotron Light Research Institute (SLRI), Thailand, in order to accommodate the wide range of absorption edge energies corresponding to the constituent elements of the samples. For Ce L_3-edge and Nb L_3-edge analyses, XAS spectra were collected in fluorescence mode at Beamline 8, covering a photon energy range of 2–6 keV. Measurements at the Pb L_3-edge and Bi L_3-edge were performed at Beamline 1.1W using a combination of transmission and fluorescence modes, with photon energies ranging from 13–19 keV.

The acquired XAS data were processed and analyzed using the ATHENA and ARTEMIS software programs within the Demeter package. These programs were utilized for background subtraction, normalization, and fitting of the XANES and EXAFS regions to extract reliable electronic and structural parameters.

3.4 Photocatalytic test

Photocatalytic performance was evaluated through the reduction of methylene blue (MB) using a solar simulation lamp as the light source. An aqueous MB solution with an initial concentration of 20 ppm was employed as a representative organic dye pollutant. For each experiment, 50 mg of photocatalyst was dispersed in 50 mL of the MB solution, resulting in a catalyst loading of 1 g/L.

Prior to light irradiation, the suspension was magnetically stirred at 400 rpm in the dark for 1 h to establish adsorption–desorption equilibrium between the MB molecules and the photocatalyst surface. This dark adsorption step ensured that subsequent changes in MB concentration were attributed solely to photocatalytic reactions rather than physical adsorption.

After the adsorption equilibrium was achieved, the suspension was irradiated under simulated solar light. During irradiation, 5 mL aliquots of the suspension were withdrawn at predetermined time intervals. The solid photocatalyst was then separated from the collected samples by centrifugation to obtain clear supernatant solutions.

The concentration of MB in the supernatant was determined by measuring the absorbance at the maximum absorption wavelength (λ_{max} = 664 nm) using a UV–visible

spectrophotometer. The photocatalytic degradation efficiency was calculated using Equation (3.2):

$$\%\text{degradation} = [(C_0 - C_t)/C_0] * 100 \quad (3.2)$$

where C_0 is the initial concentration of MB.

C_t is the concentration of MB after irradiation at time t.

3.5 Computational details

To clarify the effect of Ce doping on the electronic properties of the $PbBi_2Nb_2O_9$ structure (PBNO), we conducted first-principles calculations using density functional theory (DFT) with spin polarization, utilizing the Vienna Ab initio Simulation Package (VASP 6.3) (Kresse and Furthmüller, 1996). The interaction between core ions and electrons was modeled using the projector-augmented wave (PAW) method (Kresse and Joubert, 1999), while the exchange-correlation functional was described using the generalized gradient approximation with the Perdew-Burke-Ernzerhof (PBE) functional (Perdew, Burke and Ernzerhof, 1996).

All structures were performed the optimization with energy and force convergence criteria set at 10^{-6} eV and 0.02 eV/Å, respectively. All calculations were performed using valence-electron wavefunctions of O $2s^2$ $2p^4$, Nb $4s^2$ $4p^6$ $4d^4$ $5s^1$, Ce $4f^1$ $5s^2$ $5p^6$ $5d^1$ $6s^2$, Pb $5d^{10}$ $6s^2$ $6p^2$ and Bi $5d^{10}$ $6s^2$ $6p^3$ expanded in a plane-wave basis with energy cutoff of 500 eV. Additionally, k-points sampling of 6×6×1 and 13×13×1 grids were employed using the Monkhorst-Pack meshes (Monkhorst and Pack, 1976) for optimization and electronic density of state (DOS) calculation, respectively.

3.6 References

Kartashov, O. O., Chernov, A. V., Polyanichenko, D. S., & Butakova, M. A. (2021). XAS Data Preprocessing of Nanocatalysts for Machine Learning Applications. *Materials*. *14*(24), 7884.

Kresse, G., & Furthmüller, J. (1996). Efficiency of ab-initio total energy calculations for metals and semiconductors using a plane-wave basis set. *Computational Materials Science*. *6*(1), 15-50. doi:10.1016/0927-0256(96)00008-0.

Kresse, G., & Joubert, D. (1999). From ultrasoft pseudopotentials to the projector augmented-wave method. *Physical Review B*. *59*(3), 1758-1775. doi:10.1103/PhysRevB.59.1758.

Monkhorst, H. J., & Pack, J. D. (1976). Special points for Brillouin-zone integrations. *Physical Review B*. *13*(12), 5188-5192. doi:10.1103/PhysRevB.13.5188.

Perdew, J. P., Burke, K., & Ernzerhof, M. (1996). Generalized Gradient Approximation Made Simple. *Physical Review Letters*. *77*(18), 3865-3868. doi:10.1103/PhysRevLett.77.3865.

CHAPTER IV
RESULTS AND DISCUSSION

4.1 Crystal structure

4.1.1 Different preparation method of $PbBi_2Nb_2O_9$

The materials were synthesized using three different preparation techniques, namely the Sol–gel, Hydrothermal, and Molten salt methods. The crystalline structures of the materials obtained from each method were examined using X-ray diffraction (XRD), and the corresponding patterns are presented in Figure 4.1. The XRD results indicate that all synthesized samples exhibited diffraction peaks that are in good agreement with the standard crystalline structure of PBNO (JCPDS No. 86-1333), confirming the successful formation of the target phase regardless of the preparation method.

Although all samples showed similar phase compositions, noticeable differences were observed in the intensity and sharpness of the diffraction peaks, reflecting variations in crystallinity. The sample prepared via the Molten salt method displayed the highest peak intensities and the sharpest diffraction patterns, suggesting superior crystallinity. This was followed by the Hydrothermal method, while the Sol–gel method exhibited relatively broader and less intense peaks, indicating a lower degree of crystallinity.

The morphological characteristics of the synthesized materials were further investigated using scanning electron microscopy (SEM), as shown in Figure 4.2. The SEM images support the XRD findings, revealing that the Molten salt–derived material possessed well-defined, densely packed plate-like structures, consistent with its high crystallinity. In contrast, the Hydrothermal method resulted in uniformly distributed spherical particles that tended to aggregate into clusters. Meanwhile, the Sol–gel-prepared

material exhibited a largely amorphous morphology with an interconnected network-like structure, leading to the formation of voids within the material.

The photocatalytic performance of the materials prepared by each method was evaluated using methylene blue (MB) degradation under irradiation, as illustrated in Figure 4.3. Interestingly, despite its lower crystallinity, the Sol–gel-derived material demonstrated the highest photocatalytic activity, achieving complete degradation of MB within 60 minutes. In comparison, the materials synthesized via the Molten salt and Hydrothermal methods exhibited lower degradation efficiencies of 74% and 76%, respectively. These results suggest that factors such as surface area, porosity, and structural defects play a significant role in enhancing photocatalytic performance. Consequently, the Sol–gel preparation method was selected for further investigation in this study.

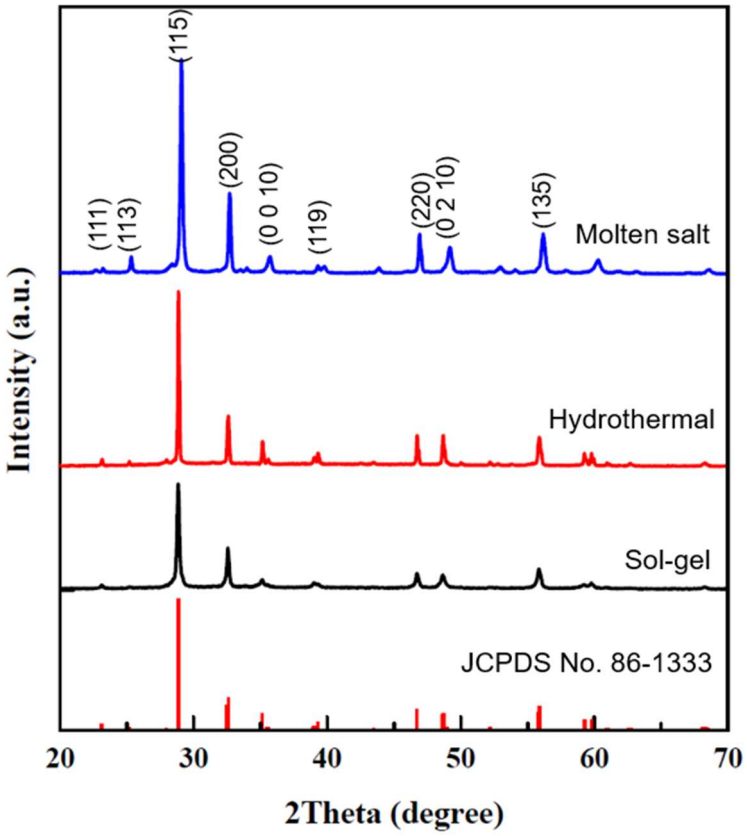


Figure 4.1 XRD patterns of $PbBi_2Nb_2O_9$ at different preparation methods Sol-gel (a), Hydrothermal (b) and Molten salt (c).

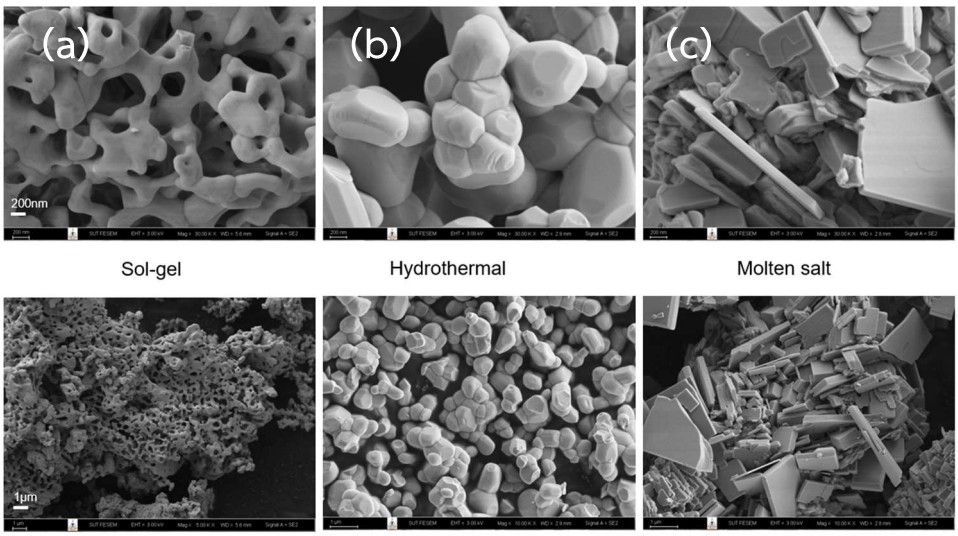


Figure 4.2 SEM images of $PbBi_2Nb_2O_9$ at different preparation methods Sol-gel (a), Hydrothermal (b) and Molten salt (c).

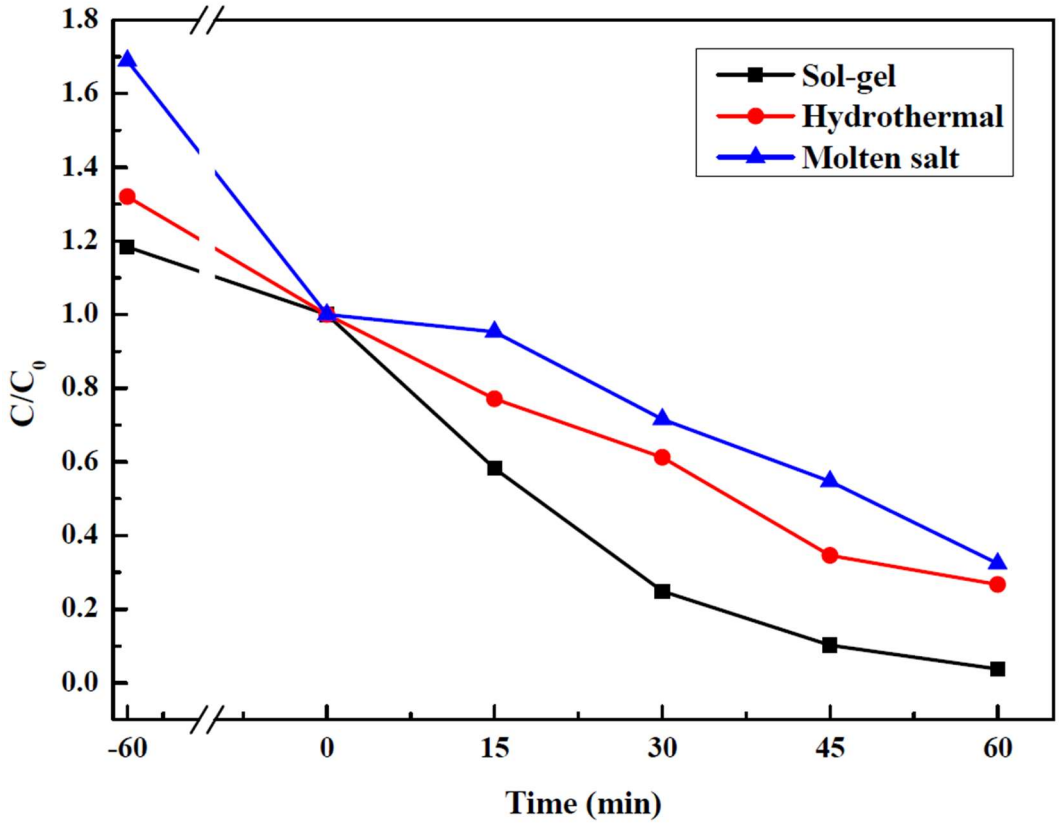


Figure 4.3 Photocatalytic degradation of $PbBi_2Nb_2O_9$ at different preparation methods.

4.1.2 Sol-Gel method by various calcination temperature

The preparation of PBNO using the Sol–gel method was further investigated by varying the calcination temperature in order to obtain a crystal structure most suitable for photocatalytic applications. Calcination was carried out at 650°C, 700°C, 750°C, and 800°C, and the resulting crystalline structures were analyzed by X-ray diffraction (XRD), as shown in Figure 4.4.

The XRD patterns indicate that all samples exhibited diffraction peaks characteristic of the Aurivillius-type structure of PBNO (JCPDS No. 86-1333). This layered structure is composed of alternating Bi_2O_2 layers and NbO_6 double-perovskite slabs stacked along the c-axis, with Pb atoms incorporated within the NbO_6 slabs. The crystal structure belongs to the orthorhombic space group $A2_1am$, with lattice parameters of a = 5.4960 Å, b = 5.4960 Å, and c = 25.5500 Å.

The principal diffraction peaks were detected at 2θ values of 23.1°, 25.1°, 28.8°, 32.5°, 35.1°, 39.3°, 46.7°, 48.7°, and 55.9°, which were indexed to the (111), (113), (115), (200), (0010), (119), (220), (0210), and (135) crystallographic planes, respectively.

Based on the analysis of the diffraction peaks, impurity phases were detected in the samples calcined at 650°C and 700°C, as evidenced by additional peaks that were not present in the standard pattern. In contrast, the samples calcined at 750°C and 800°C exhibited diffraction patterns that matched well with the standard PBNO structure, indicating the formation of a single-phase, highly crystalline material. Consequently, the PBNO sample calcined at 750°C was selected for further study, as phase purity was achieved at a lower calcination temperature, thereby reducing energy consumption compared to calcination at 800°C.

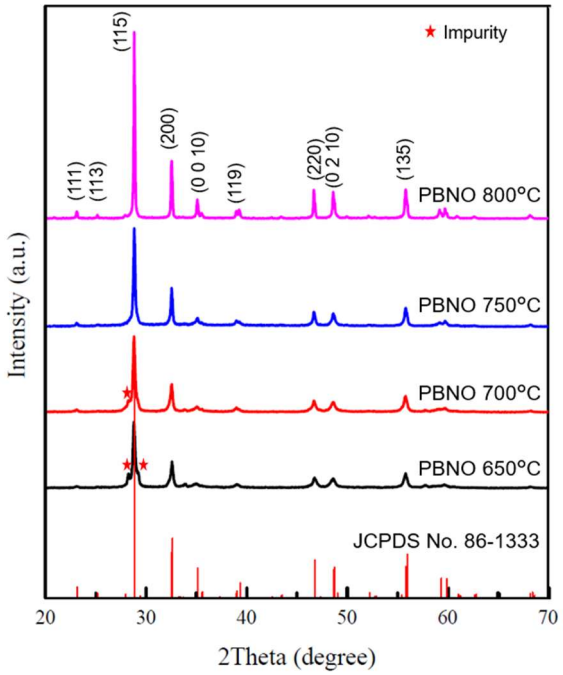


Figure 4.4 XRD patterns of $PbBi_2Nb_2O_9$ at temperatures of 650°C, 700°C, 750°C and 800°C.

4.2 Ce-doped

4.2.1 Crystal structure of Ce-doped obtained samples

$PbBi_{2-x}Ce_xNb_2O_9$ (x = 0.00, 0.05, 0.20, and 0.50) samples were synthesized using the Sol–gel method, and their crystalline structures were characterized by X-ray diffraction (XRD), as presented in Figure 4.5a. The XRD results show that the diffraction peaks of all samples could be indexed to the Aurivillius-type structure of PBNO (JCPDS No. 86-1333), which crystallizes in the orthorhombic space group $A2_1am$.

For the compositions with x = 0.00 and x = 0.20, the XRD patterns exhibited a single-phase Aurivillius two-layer structure without any detectable secondary phases, indicating successful incorporation of Ce into the PBNO lattice at these doping levels. In contrast, for the samples with x = 0.05 and x = 0.50, additional diffraction peaks were observed, suggesting the formation of unidentified impurity phases and indicating that phase stability was disrupted at these compositions.

As shown in Figure 4.5b, an enlarged view of the diffraction patterns in the 2θ range of 28.0°–33.0° highlights the reflections corresponding to the (115) and (200) crystallographic planes. With increasing Ce content, a noticeable shift of the (115) diffraction peak toward lower 2θ values was observed, while the (200) peak shifted toward higher 2θ values. These opposite peak shifts indicate changes in the lattice spacing and confirm that Ce incorporation significantly influences the unit cell parameters of $PbBi_2Nb_2O_9$, as summarized in Table 4.1.

During the calcination process, partial oxidation of Ce^{3+} to Ce^{4+} is known to occur. The substitution of Pb^{2+} ions (ionic radius = 1.49 Å, coordination number (CN) = 12) by smaller Ce^{4+} (1.14 Å, CN = 12) and/or Ce^{3+} (1.34 Å, CN = 12) ions results in a contraction of the lattice parameters a and b. This contraction is attributed to the shrinkage of the NbO_6 octahedra within the perovskite slabs. Conversely, as confirmed by additional characterization discussed later, charge compensation and cation redistribution lead to the partial occupation of Bi^{3+} sites (ionic radius = 1.17 Å, CN = 8) by larger Pb^{2+} ions (1.29 Å, CN = 8), which contributes to lattice expansion along the c-axis.

Furthermore, the reduction in octahedral size and the associated lattice strain induce distortion within the ab plane, causing the crystal structure to become increasingly orthorhombic as the Ce concentration increases. This structural distortion was quantitatively evaluated using the orthorhombicity ratio, $|(a - b)/(a + b)|$, and the calculated values are provided in Table 4.1.

Local structural changes in the samples were investigated using Fourier-transform Raman (FT-Raman) spectroscopy. The spectra were recorded in the wavenumber range of 1100–50 cm^{-1} in order to analyze vibrational modes associated with the crystal structure. The observed Raman bands were predominantly associated with the orthorhombic phase of the PBNO compound, confirming consistency with the structural information obtained from XRD analysis.

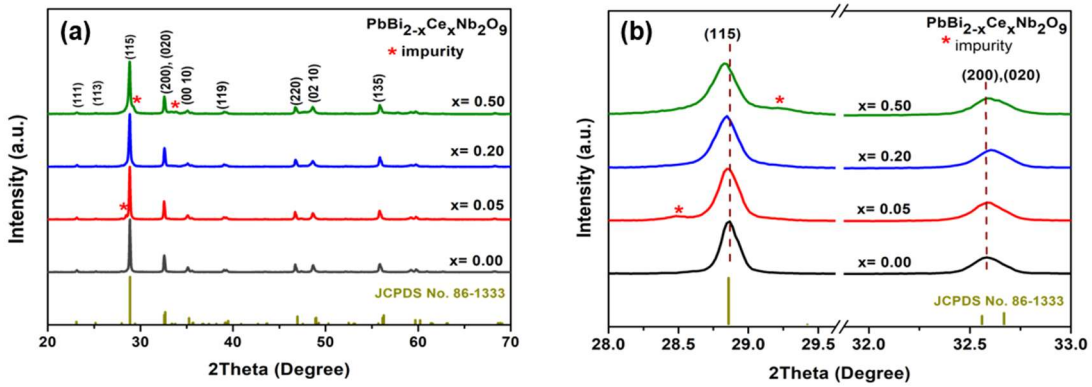


Figure 4.5 XRD patterns (a) and their close-up (b) of $PbBi_2Nb_2O_9$ (x = 0.00, 0.05, 0.20, and 0.50).

Table 4.1 Cell Parameters, Cell Volumes (V), and degree of distortion in terms of the orthorhombicity ratio (| (*a* - *b*) / (*a* + *b*) |).

Composition (x)	Cell parameter (Å)			Cell Volume; V (Å^3)	| (*a* - *b*) / (*a* + *b*) |
	a	*b*	*c*		
0.00	5.495 (2)	5.497 (1)	25.539 (2)	771.4 (3)	1.82 x 10^{-4}
0.05	5.492 (6)	5.496 (1)	25.540 (1)	770.9 (1)	3.64 x 10^{-4}
0.20	5.488 (1)	5.494 (1)	25.582 (3)	771.3 (1)	5.46 x 10^{-4}
0.50	5.486 (2)	5.488 (2)	25.586 (4)	770.3 (4)	1.82 x 10^{-4}

For the Aurivillius-type structure, Raman modes located below 200 cm^{-1} were attributed to lattice vibrations involving the Bi_2O_2 layers and the vibrations of heavy A-site cations within the perovskite blocks. These low-frequency modes are highly sensitive to distortions and cation substitutions occurring in the layered structure. In contrast, the Raman modes appearing above 200 cm^{-1} were assigned to the bending and stretching vibrations of the BO_6 octahedra in the perovskite slabs, which provide direct information about octahedral connectivity and local symmetry.

To obtain quantitative information on the vibrational behavior, the Raman spectra were deconvoluted using Lorentzian fitting, as illustrated in Figure 4.6. The extracted peak positions are summarized in Table 4.2. Variations in peak positions and

intensities reflect changes in bond lengths, bond angles, and local lattice distortions, thereby providing insight into the structural modifications induced by compositional variation.

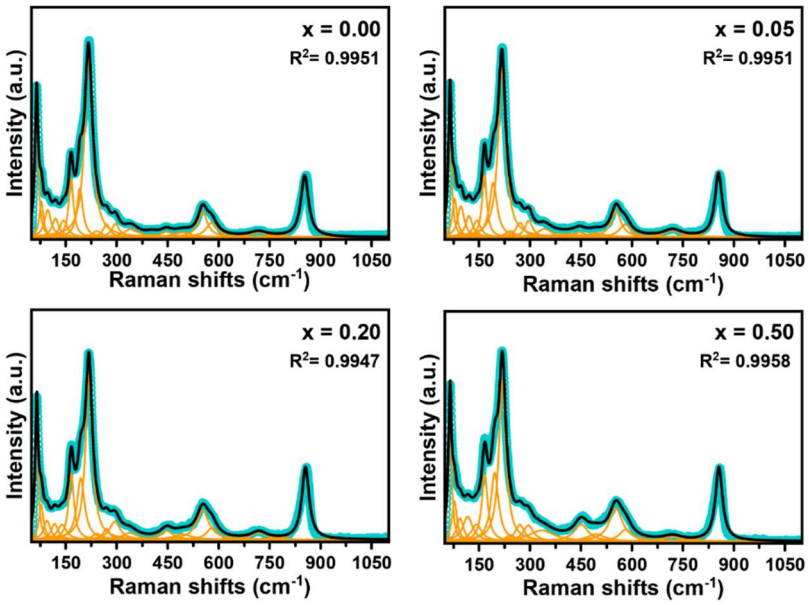


Figure 4.6 The fitted FT-Raman of $PbBi_{2-x}Ce_xNb_2O_9$ (x = 0.00, 0.05, 0.20, and 0.50).

Table 4.2 Assignment of Raman active modes of $PbBi_{2-x}Ce_xNb_2O_9$.

$PbBi_{2-x}Ce_xNb_2O_9$				assignment
x = 0.00	x = 0.05	x = 0.20	x =0.50	
64.37	64.59	64.77	64.68	Bi_2O_2 rigid layer mode
165.61	165.99	166.29	166.78	Perovskite layer A-site ion
218.67	218.44	218.27	217.88	Torsional bending of BO_6
552.83	552.54	552.93	552.76	Asymmetric B-O stretching (apical oxygen atoms)
853.15	854.59	855.45	855.87	Symmetric B-O stretching (equatorial oxygen atoms)

At a frequency of approximately 64 cm^{-1}, a vibrational mode associated with the motion of the Bi_2O_2 layers parallel to the z-axis was observed. Compared to undoped $PbBi_2Nb_2O_9$, this mode exhibited a slight shift toward higher frequencies with increasing Ce content. This frequency shift is indicative of partial occupation of Pb^{2+} ions within the Bi_2O_2 layers, which modifies the local bonding environment. The frequency of this vibrational mode is governed by the effective mass of the vibrating cation and the strength of the metal–oxygen (M–O) bond. Although Bi^{3+} and Pb^{2+} possess similar atomic masses (209 amu for Bi^{3+} and 207 amu for Pb^{2+}), Bi–O bonds exhibit a lower bond dissociation energy (337 kJ/mol) than Pb–O bonds (382 kJ/mol). Consequently, the partial replacement of Bi^{3+} by Pb^{2+} within the Bi_2O_2 layers results in an increase in bond strength, leading to a shift of the vibrational mode toward higher wavenumbers.

In addition, a high-intensity Raman band located at approximately 165 cm^{-1}, which is associated with vibrations of A-site cations within the perovskite-like layers, was observed to shift toward higher frequencies as the Ce content increased. This behavior is attributed to variations in the A–O bond strength resulting from the substitution of Ce ions, which possess stronger Ce–O bonding (795 kJ/mol), for Pb^{2+} ions. The enhanced bond strength leads to stiffer lattice vibrations and consequently higher Raman frequencies.

The counter-motion vibrations of the NbO_6 octahedra were identified by Raman bands located at approximately 217 cm^{-1}, 552 cm^{-1}, and 854 cm^{-1}. The vibrational mode at 217 cm^{-1} was assigned to the bending vibration of the NbO_6 octahedra and is commonly regarded as a sensitive indicator of octahedral distortion. With increasing Ce concentration, this mode exhibited a shift toward higher wavenumbers, suggesting an increase in the distortion of the NbO_6 octahedra induced by Ce substitution. This observation is in good agreement with previously reported studies on doped Aurivillius-type materials.

The Raman band observed at approximately 552 cm^{-1} was attributed to the asymmetric stretching vibration of Nb–O bonds involving the terminal oxygen atoms, while the band at approximately 854 cm^{-1} originated from the symmetric stretching vibration of Nb–O bonds along the z-axis of the crystal lattice. These vibrations correspond to oxygen atoms located along the centerline of the NbO_6 octahedra. As shown in Figure 4.7a, the band associated with the symmetric Nb–O stretching mode shifted progressively toward higher wavenumbers with increasing Ce content. This shift indicates a shortening of the Nb–O bond length, which is influenced by the incorporation of Ce ions at the A-site of the perovskite-like layers.

According to the empirical relationship proposed by Hardcastle, the Nb–O bond distance (R_{Nb-O}) can be correlated with the Raman stretching frequency using the following equation (4.1):

$$R_{Nb-O} = 0.5217 \ln(25922/ \mathbf{V}) \quad (4.1)$$

where **V** represents the Raman stretching frequency in units of cm^{-1}. The calculated bond lengths, shown in Figure 4.7b, indicate that the Nb–O bond lengths associated with equatorial oxygen atoms decrease systematically with increasing Ce content, whereas the Nb–O bond lengths corresponding to apical oxygen atoms remain nearly unchanged. Furthermore, the reduction in equatorial Nb–O bond lengths is consistent with the FT-IR results (Figure 4.7c) and XRD analysis, and it supports the observed decrease in the lattice parameters within the ab plane. This behavior is attributed to the contraction of the NbO_6 octahedra resulting from Ce-induced structural distortion.

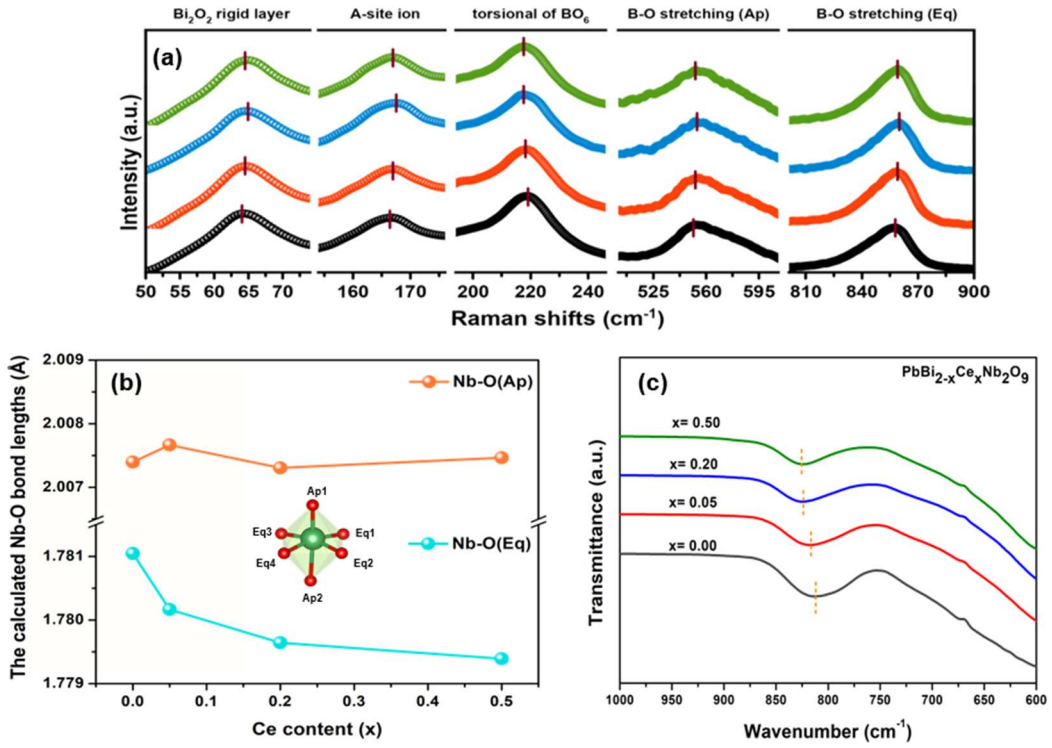


Figure 4.7 The FT-Raman spectra (a), the calculated Nb–O bond lengths (b) and FT-IR spectra (c) of $PbBi_{2-x}Ce_xNb_2O_9$ (x = 0.00, 0.05, 0.20, and 0.50).

4.2.2 Morphology and surface area

The structural characteristics of PBNO and Ce-doped PBNO samples were examined using scanning electron microscopy (SEM), high-resolution transmission electron microscopy (HRTEM), selected area electron diffraction (SAED), and energy-dispersive X-ray spectroscopy (EDS). The SEM images reveal that the morphology of PBNO is irregular and is significantly influenced by the incorporation of Ce, as shown in Figure 4.8. With increasing Ce concentration, a noticeable change in particle morphology and crystallinity was observed.

For the undoped PBNO sample, the SEM image (Figure 4.8a) reveals a porous microstructure composed of interconnected pores, which is favorable for mass transport. At the nanoscale, the HRTEM image (Figure 4.8b) shows well-defined lattice fringes with an interplanar spacing of approximately 0.27 nm, corresponding to the

(200) and (020) crystal planes of PBNO. This observation indicates the presence of a well-ordered crystalline structure. The corresponding SAED pattern (Figure 4.8c) exhibits sharp and discrete diffraction spots, confirming the single-crystalline nature of the PBNO sample. The measured angle of approximately 90° between the (200) and (020) diffraction spots is consistent with the theoretical value expected for an orthorhombic crystal structure, further validating the structural integrity of the undoped PBNO.

In contrast, the $PbBi_{1.8}Ce_{0.2}Nb_2O_9$ sample exhibits a markedly different morphology, as shown in Figure 4.8d. The SEM image reveals the formation of larger, well-defined grains, accompanied by the presence of small particles distributed on the surface of the grains. This morphological evolution suggests that Ce incorporation influences nucleation and grain growth during the synthesis process. HRTEM analysis of these small surface particles (Figure 4.8e) reveals lattice spacings of approximately 0.31 nm and 0.27 nm, which can be indexed to the (115) and (200) crystallographic planes, respectively. These results indicate that the Ce-doped sample retains the Aurivillius-type crystal structure at the nanoscale, despite the observed changes in morphology.

The SAED pattern obtained from the $PbBi_{1.8}Ce_{0.2}Nb_2O_9$sample (Figure 4.8f) exhibits concentric diffraction rings rather than discrete spots, which is characteristic of a polycrystalline structure and indicates a reduction in crystallinity compared to the undoped PBNO sample. Nevertheless, EDS elemental mapping (Figure 4.8g) confirms that Pb, Bi, Ce, Nb, and O are uniformly distributed throughout the $PbBi_{1.8}Ce_{0.2}Nb_2O_9$ sample, demonstrating successful and homogeneous incorporation of Ce into the PBNO lattice.

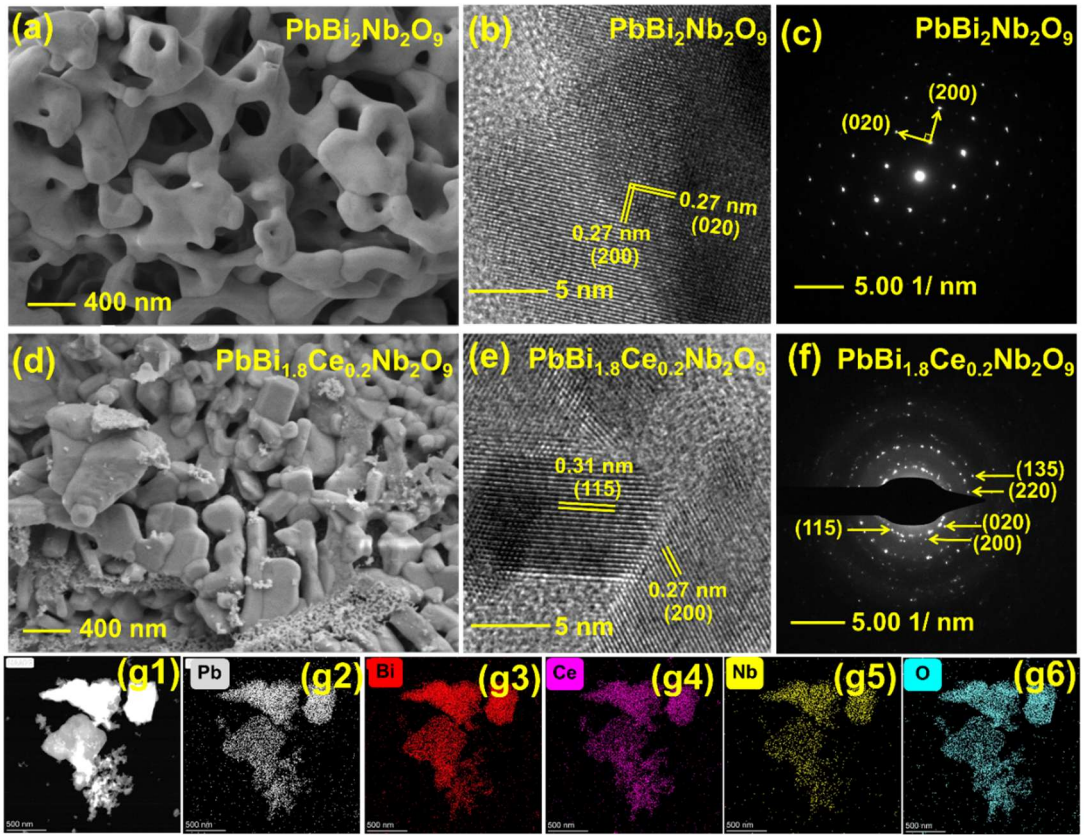


Figure 4.8 SEM (a and d), HRTEM (b and e), SAED pattern (c and f) of $PbBi_2Nb_2O_9$ and $PbBi_{1.8}Ce_{0.2}Nb_2O_9$, and EDS of $PbBi_{1.8}Ce_{0.2}Nb_2O_9$ (g1-g6).

The specific surface areas of all samples were determined using the Brunauer–Emmett–Teller (BET) method based on nitrogen adsorption–desorption measurements. The corresponding N_2 adsorption–desorption isotherms are presented in Figure 4.9. A noticeable increase in the specific surface area was observed for the Ce-doped samples compared to the undoped PBNO sample.

The enhancement in surface area suggests that the incorporation of Ce significantly alters the morphology and surface texture of PBNO. This morphological modification is consistent with the microstructural changes observed in the SEM and HRTEM analyses, where Ce doping was shown to promote grain growth accompanied by the formation of surface-attached nanoparticles and microstructural heterogeneity.

As a result, an increased number of exposed surface sites is generated, despite the observed reduction in long-range crystallinity.

From a photocatalytic perspective, the increase in specific surface area is particularly advantageous, as it provides a larger number of active sites for the adsorption of reactant molecules and facilitates more effective interaction between the photocatalyst surface and incident light. Consequently, the enhanced surface area induced by Ce substitution is expected to contribute positively to the photocatalytic performance of PBNO by improving reactant accessibility and promoting surface-mediated photocatalytic reactions.

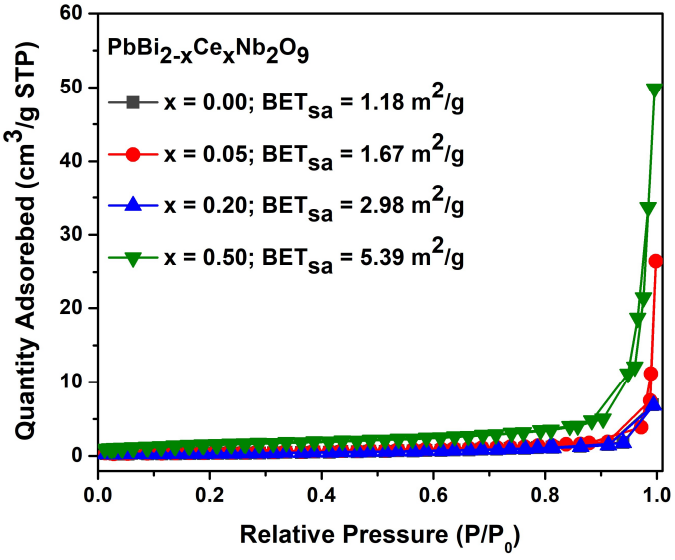


Figure 4.9 Nitrogen adsorption–desorption isotherm and surface area of $PbBi_{2-x}Ce_xNb_2O_9$.

4.2.3 Electronic band structure and band gap energy

The electronic band structure and band gap energy, which are strongly influenced by ion substitution and play a crucial role in determining photocatalytic activity, were investigated using optical absorption data obtained from UV–visible diffuse reflectance spectroscopy (UV–vis DRS), as shown in Figure 4.10a. The optical band gap energies were estimated by extrapolating the linear region of the Kubelka–

Munk plots of $[F(R)h\nu]^{1/2}$versus photon energy (h$\mathbf{V}$), assuming an indirect allowed electronic transition. In this analysis, $F(R)$represents the Kubelka–Munk function, defined as $F(R) = (1-R)^2/2R$, where R corresponds to the reflectance ratio of the sample relative to the standard reference.

The calculated band gap energies of all samples are summarized in Figure 4.10b. A systematic reduction in band gap energy was observed upon Ce doping, accompanied by enhanced light absorption in the visible region. This red-shift in the absorption edge indicates that Ce incorporation effectively extends the optical response of PBNO toward longer wavelengths. As a result, improved utilization of visible light is enabled, which is expected to enhance photocatalytic performance, as materials with narrower band gaps generally exhibit higher photocatalytic efficiency under visible-light irradiation.

In addition to experimental optical analysis, the influence of Ce doping on the electronic structure was further elucidated through density of states (DOS) calculations. The calculated DOS of pure PBNO is shown in Figure 4.10c, while that of Ce-doped PBNO is presented in Figure 4.10d. For the undoped PBNO, the DOS exhibits symmetric distributions between spin-up and spin-down states, indicating a non-magnetic electronic character. The valence band maximum (VBM) was found to be predominantly composed of O 2p states, whereas the conduction band minimum (CBM) mainly consists of Nb 4d states.

In contrast, the DOS of Ce-doped PBNO exhibits asymmetry in the conduction band region, reflecting modifications to the electronic structure induced by Ce incorporation. Although the VBM remains dominated by O 2p states, the CBM is now contributed by both Nb 4d and Ce 4f states. The introduction of Ce-derived electronic states near the CBM leads to a reduction in the band gap energy by lowering the CBM energy level. This downward shift of the CBM is attributed to the hybridization and interaction between Nb 4d and Ce 4f orbitals, which alters the electronic band alignment.

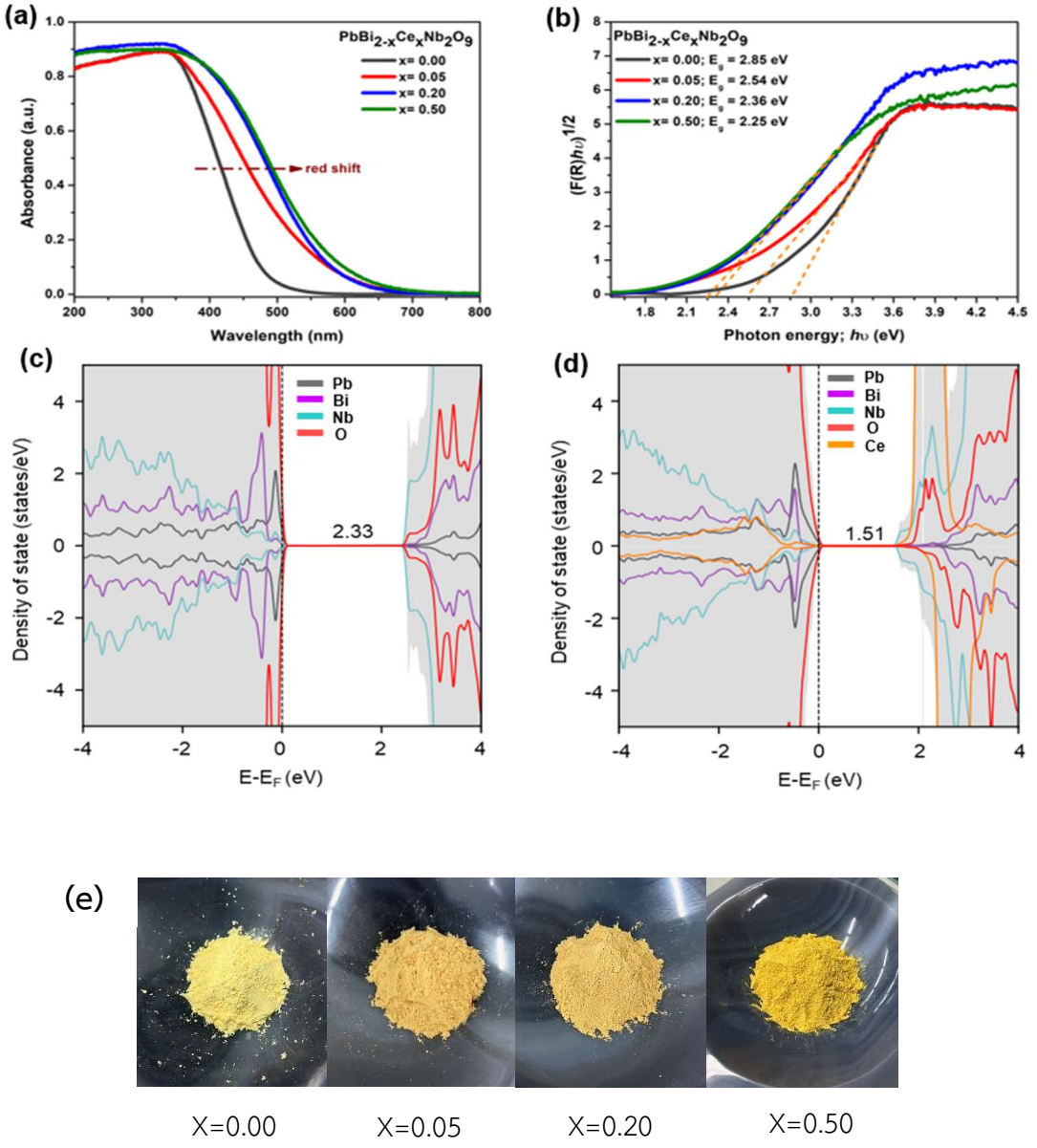


Figure 4.10 UV-vis absorption spectra (a) and Kubelka–Munk plot (b) of $PbBi_{2-x}Ce_xNb_2O_9$ (x = 0.00, 0.05, 0.20, and 0.50). The density of state (DOS) of (c) pure and (d) Ce-doped $PbBi_2Nb_2O_9$**.** The colour of obtained photocatalysts (e).

Furthermore, a detailed analysis of the band structure reveals changes in orbital hybridization at the valence band edge in the Ce-doped samples, as shown in Figure 4.11a–b. In particular, variations in Pb orbital contributions at the VBM were observed. These changes are associated with modifications in the local coordination

environment, including variations in Pb–O bond lengths and bond angles at both the original Pb sites and substituted Bi sites. Such structural distortions, induced by Ce doping and cation redistribution, enhance orbital overlap and further influence the electronic band structure. These observations highlight the strong coupling between lattice disorder, cation substitution, and electronic structure in Ce-doped PBNO.

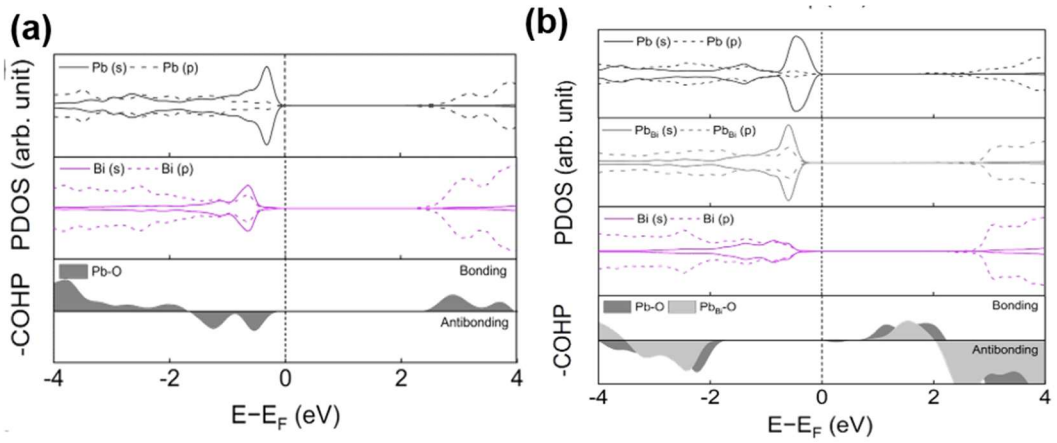


Figure 4.11 Projected electronic density of states (PDOS) of s and p orbital of Pb and Ce and crystal orbital Hamilton populations (COHP) for Pb-O and Pb_{Bi}-O of (a) pure and (b) Ce-doped $PbBi_2Nb_2O_9$.

4.2.4 Chemical state

The chemical states and elemental compositions of the samples with x = 0.00 and x = 0.20 were analyzed by X-ray photoelectron spectroscopy (XPS). The survey XPS spectra, as shown in Figure 4.12a, confirm the presence of Pb, Bi, Nb, and O elements in the undoped $PbBi_2Nb_2O_9$ sample, while additional characteristic peaks corresponding to Ce are observed in the Ce-doped sample, indicating the successful incorporation of Ce into the PBNO lattice.

The high-resolution Ce 3d core-level XPS spectrum of the x = 0.20 sample is presented in Figure 4.12b. The spectrum was deconvoluted into ten characteristic peaks, revealing the coexistence of Ce^{3+} and Ce^{4+} oxidation states. The peaks labeled as *v*, *v*'', *v*''', *u*, *u*'' and *u*''' are recognized as fingerprints of Ce^{4+} species, whereas

the remaining peaks are attributed to Ce^{3+} species, in agreement with previously reported studies (Soni et al., 2018) (Yang et al., 2020). The absence of Ce 3d signals in the undoped PBNO sample further confirms that Ce is exclusively introduced through doping.

The high-resolution Bi 4f spectrum (Figure 4.12c) exhibits two prominent peaks corresponding to Bi $4f_{7/2}$ and Bi $4f_{5/2}$ with binding energies in the ranges of 159.14–159.44 eV and 164.44–164.75 eV, respectively. These values are characteristic of Bi^{3+} species and indicate that the valence state of Bi remains unchanged after Ce doping. Similarly, the Pb 4f spectrum (Figure 4.12d) displays Pb $4f_{7/2}$ and Pb $4f_{5/2}$ peaks at binding energies consistent with Pb^{2+}, confirming the preservation of the Pb oxidation state. The Nb 3d core-level spectrum (Figure 4.12e) shows Nb $3d_{5/2}$ and Nb $3d_{3/2}$ peaks located at 206.62–206.79 eV and 209.37–209.56 eV, respectively, which are characteristic of Nb^{5+} species, indicating that the Nb oxidation state is also maintained upon Ce incorporation.

The O 1s spectrum (Figure 4.12f) was deconvoluted into three distinct components. The peak at lower binding energy is assigned to lattice oxygen (O_L), the intermediate peak corresponds to surface-adsorbed oxygen species (O_{ads}), and the peak at higher binding energy is attributed to molecularly adsorbed water (O_{H2O}) on the surface. A slight shift of the O 1s peak toward lower binding energies was observed for the Ce-doped sample compared to the undoped PBNO. This shift is attributed to changes in the local electronic environment resulting from the incorporation of mixed-valence Ce^{3+}/Ce^{4+} ions, which alter the ionicity and electronic polarizability of the metal–oxygen bonds within the lattice.

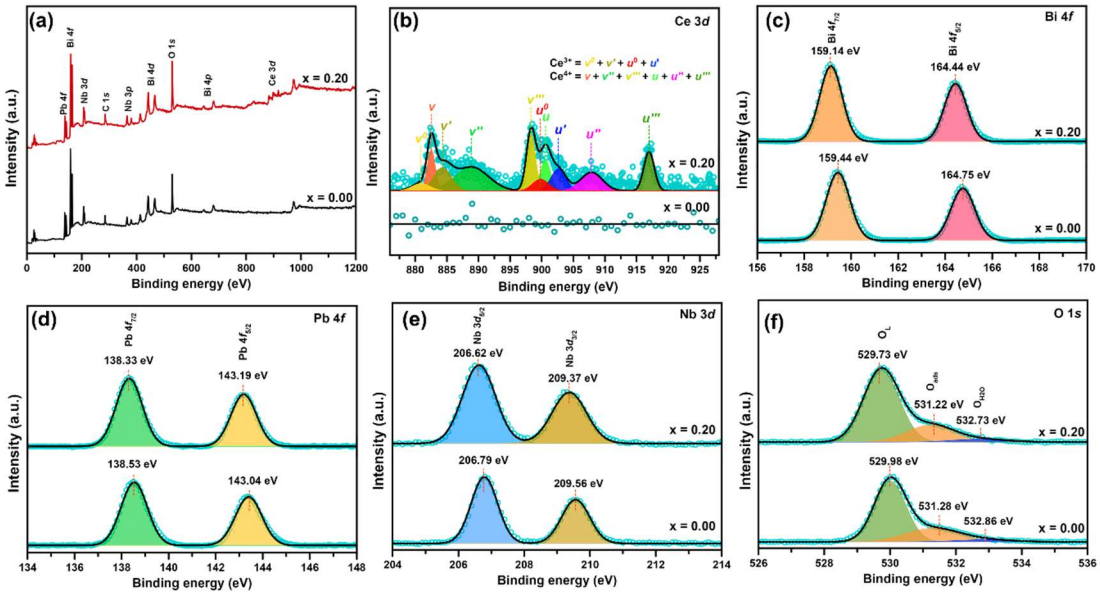


Figure 4.12 XPS spectrum:(a) survey spectra, and high-resolution spectrum of (b) Ce 3d, (c) Bi 4*f*, (d) Pb 4*f*, (e) Nb 3d, and (f) O 1*s* of $PbBi_{2-x}Ce_xNb_2O_9$ (x = 0.00, and 0.20).

The chemical-state information obtained from XPS analysis can be further corroborated and complemented by X-ray absorption spectroscopy (XAS), which provides insight into the bulk electronic structure and local coordination environment of the constituent elements. While XPS is a surface-sensitive technique probing the top few nanometers of the material, XAS offers element-specific information representative of the bulk, thereby enabling a comprehensive understanding of the oxidation states and electronic structure of Ce-doped PBNO (Watts J, 2003).

The XPS results reveal the coexistence of Ce^{3+} and Ce^{4+} species in the Ce-doped PBNO sample, as evidenced by the deconvolution of the Ce 3d core-level spectrum. This mixed-valence behavior is consistent with the XAS spectra at the Ce L_3-edge (Figure 4.13d), where characteristic absorption features corresponding to both Ce^{3+} and Ce^{4+} states are typically observed (Mullins, 2015). In XAS, the presence of multiple white-line features and changes in edge intensity and shape reflect variations in the Ce 4f occupancy, thereby confirming the mixed-valence nature of Ce within the PBNO lattice.

Furthermore, the stability of the Pb^{2+}, Bi^{3+} and Nb^{5+} oxidation states inferred from XPS core-level binding energies is supported by XAS measurements at the Pb L_3-edge, Bi L_3-edge and Nb L_3-edge as show in Figure4.13(a)-(c), respectively. The absence of significant edge shifts or changes in the near-edge structure indicates that the electronic states of these host cations remain largely unaffected upon Ce substitution (Mizoguchi and Woodward, 2004). This agreement between XPS and XAS confirms that Ce substitution does not induce redox changes in the Bi, Pb, or Nb species, but instead primarily affects the local electronic environment through defect formation and orbital hybridization.

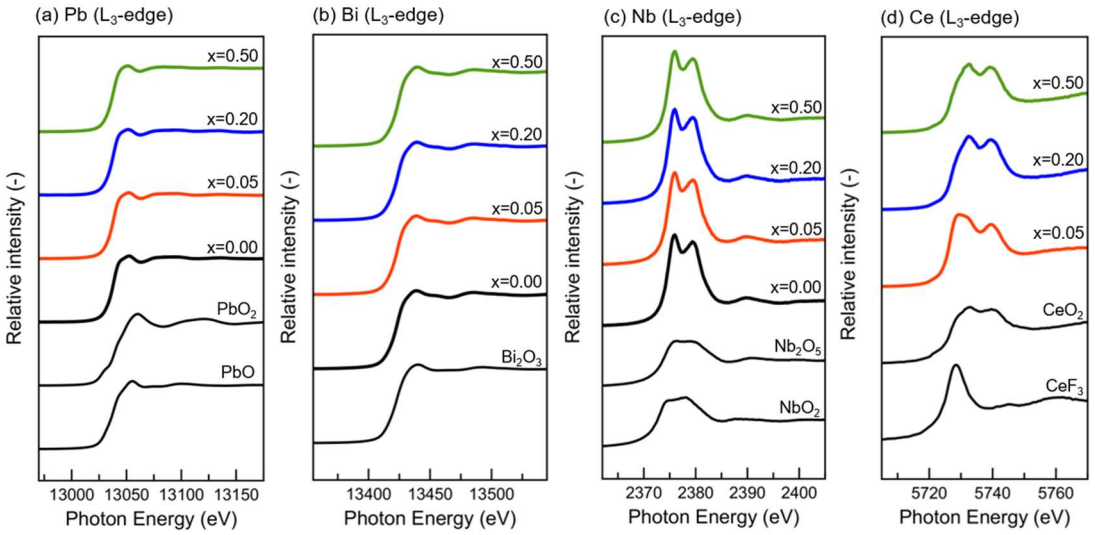


Figure 4.13 XANES spectrum: (a) Pb (L_3-edge), (b) Bi (L_3-edge), (c) Nb (L_3-edge) and (d) Ce (L_3-edge) of $PbBi_{2-x}Ce_xNb_2O_9$ (x = 0.00, 0.05, 0.20, and 0.50).

Overall, the combined XPS and XAS analyses demonstrate that Ce incorporation introduces mixed-valence Ce species and modifies the local electronic structure without altering the oxidation states of the host lattice cations. XPS provides direct evidence of surface chemical states and defect-related oxygen species, while XAS confirms the bulk electronic configuration and orbital hybridization effects. This complementary interpretation reinforces the conclusion that the enhanced photocatalytic performance of Ce-doped PBNO arises from the synergistic effects of

mixed-valence Ce, modified metal–oxygen bonding, and electronic band structure tailoring (Zhang, Zhao, Díaz-Somoano, Yang and Zhang, 2018).

4.3 Photocatalytic activity

The photocatalytic performance was evaluated through the degradation of methylene blue (MB) under simulated solar light irradiation, a method commonly used to assess the activity of semiconductor photocatalysts due to the stability and well-defined optical properties of MB (Hoffmann, Martin, Choi and Bahnemann, 1995). Enhanced photocatalytic activity was observed for PBNO at pH 12, which was attributed to the increased generation of hydroxyl radicals ($^{\cdot}OH$) and improved adsorption of MB molecules under alkaline conditions (Figure 4.14a). Under basic environments, the higher concentration of OH^{-} ions promote the formation of $^{\cdot}OH$ radicals, which are recognized as the primary oxidative species responsible for organic dye degradation (Chong, Jin, Chow and Saint, 2010; Herrmann, 1999). Consequently, a basic condition (pH 12) was selected to investigate the influence of Ce substitution on the photocatalytic performance, as illustrated in Figure 4.14b.

In the presence of Ce dopants, the degradation behavior of MB for all samples was analyzed using pseudo-first-order kinetics based on the Langmuir–Hinshelwood model, which is widely applied to heterogeneous photocatalytic reactions at low pollutant concentrations (Linsebigler, Lu and Yates Jr, 1995). The kinetic relationship is expressed by Equation (4.2):

$$\ln(C_0/C) = kt \tag{4.2}$$

where C_0 and C represent the MB concentration at the initial state and at time t, respectively, and k is the apparent rate constant (min^{-1}).

The kinetic analysis derived from the pseudo-first-order model (Figure 4.14c) reveals that an optimal Ce doping level of 0.2 was achieved. The $PbBi_{1.8}Ce_{0.2}Nb_2O_9$

sample exhibited a photocatalytic efficiency approximately 2.6 times higher than that of pristine PBNO. This enhancement can be attributed to improved charge carrier separation and the suppression of electron–hole recombination induced by appropriate Ce incorporation into the lattice (Zhang and Nosaka, 2014). In contrast, samples with Ce contents of x=0.05 and x=0.50 demonstrated lower photodegradation efficiencies than pure $PbBi_2Nb_2O_9$. Such deterioration in activity is likely related to the formation of impurity phases or excessive defect states, which act as recombination centers and hinder the photocatalytic process, resulting in reduced photodegradation efficiency (Somorjai, 1977).

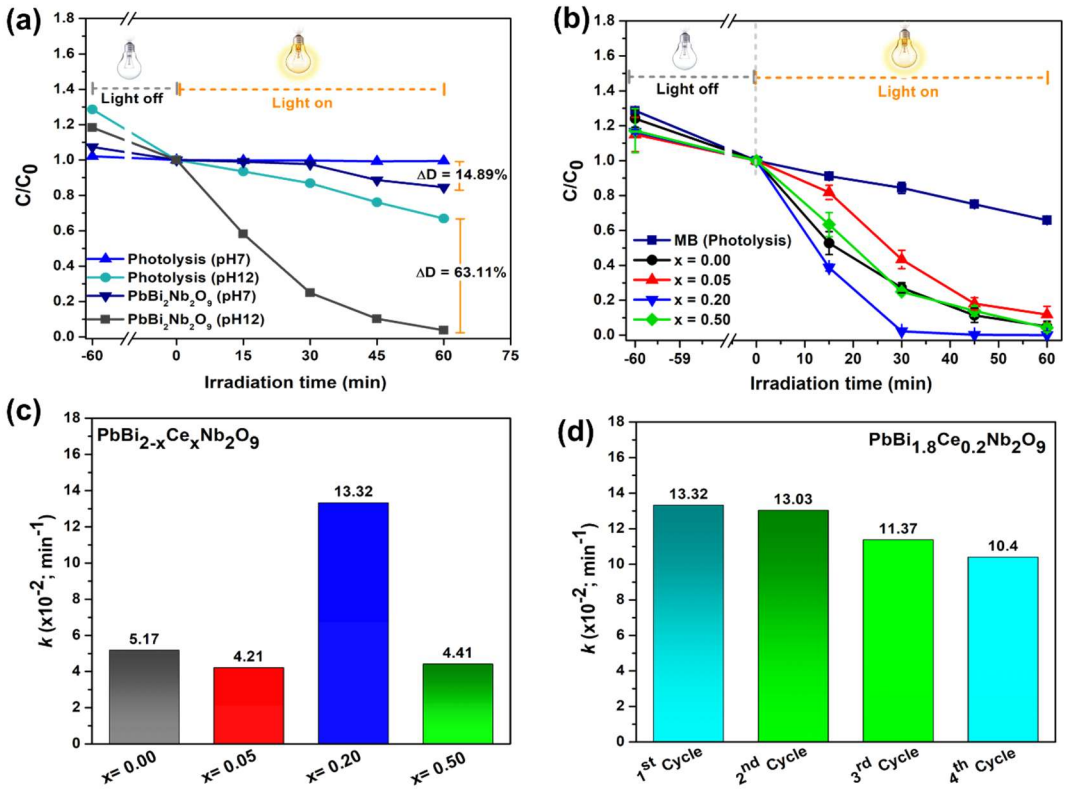


Figure 4.14 Photolysis and photocatalytic activity of $PbBi_2Nb_2O_9$ between pH7 and 12 (a), The photocatalytic activities (b) and the percentages of MB degradation and the rate constants of the apparent pseudo first order reaction (c) at pH12 of $PbBi_{2-x}Ce_xNb_2O_9$. Cycling experiment of the photocatalytic degradation MB on $PbBi_{1.8}Ce_{0.2}Nb_2O_9$ (d).

In addition to enhanced photocatalytic activity, $PbBi_{1.8}Ce_{0.2}Nb_2O_9$ exhibited satisfactory cyclic stability. After four successive photocatalytic cycles, approximately 99% MB degradation was achieved within 60 minutes, corresponding to a rate constant of $10.4x10^{-2}$ min^{-1}, as presented in Figure 4.14d. The retention of high activity over repeated cycles indicates good structural stability and reusability, which are essential for practical photocatalytic applications (Chen and Mao, 2007).

Although variations in band gap energy, morphology, and specific surface area were observed to contribute to the enhanced photocatalytic activity of the Ce-doped samples, these factors alone were insufficient to fully explain the observed performance trends. The efficiency of photogenerated electron–hole pair separation was therefore considered a critical parameter governing the overall photocatalytic behavior of the catalysts. Consequently, photoluminescence (PL) spectroscopy was employed to evaluate the separation efficiency of photogenerated charge carriers in the synthesized samples.

As presented in Figure 4.15a, the Ce-doped samples exhibited significantly lower PL intensities than pristine PBNO, while the main emission peaks remained at similar positions. This observation indicates that radiative recombination was effectively suppressed upon Ce incorporation, suggesting that the separation efficiency of photogenerated electron–hole pairs was enhanced due to the presence of Ce^{3+}/Ce^{4+} ions (Huang et al., 2014). Among the investigated compositions, $PbBi_{1.80}Ce_{0.20}Nb_2O_9$ demonstrated the lowest PL intensity, indicating the highest charge separation efficiency within the series.

The enhanced charge separation observed for the optimally doped sample was attributed to two primary factors. First, the coexistence of the Ce^{3+}/Ce^{4+} redox couple was found to facilitate reversible electron trapping and release, thereby prolonging the lifetime of charge carriers. Second, lattice distortions induced by Ce substitution, particularly within the NbO_6 octahedra, were shown to generate additional defect states that function as electron-trapping sites (Li, Chen, Zhang and Lv, 2010). These

combined effects contribute to the suppression of electron–hole recombination and promote improved photocatalytic performance.

It is important to note that an optimal Ce doping concentration is required to maximize photocatalytic efficiency (Dai et al., 2016). In the case of $PbBi_{1.95}Ce_{0.05}Nb_2O_9$, the low Ce content provided limited enhancement in charge separation, while the formation of secondary phases further reduced photocatalytic activity. Conversely, excessive Ce incorporation, particularly in the $PbBi_{1.5}Ce_{0.5}Nb_2O_9$ composition, resulted in the introduction of a high density of defect states, mainly associated with Ce^{4+} species. These defects acted as recombination centers, thereby accelerating charge carrier recombination and diminishing photocatalytic efficiency (Vento-Lujano and González, 2021).

To further understand the charge carrier dynamics, the time-resolved photoluminescence (TRPL) spectra of pure $PbBi_2Nb_2O_9$ and Ce-doped $PbBi_{1.80}Ce_{0.20}Nb_2O_9$ were recorded, as shown in Figure 4.15b. The obtained PL decay profiles were satisfactorily fitted using a triple-exponential decay function, which is described by Equation (4.3):

$$I(t)=A_1\exp(-t/\tau_1)+A_2\exp(-t/\tau_2)+A_3\exp(-t/\tau_3) \quad (4.3)$$

where ($\boldsymbol{\tau}_i$) represents the decay lifetime of the *i*-th component and A_i represents the corresponding amplitude. The average PL lifetime ($\boldsymbol{\tau}_{avg}$) were estimated with the $\boldsymbol{\tau}_i$ and A_i values from the fitted curves data according to equation (4.4):

$$\boldsymbol{\tau}_{avg}=\frac{A_1\tau_1^2+A_2\tau_2^2+A_3\tau_3^2}{A_1\tau_1+A_2\tau_2+A_3\tau_3} \quad (4.4)$$

The detailed fitting parameters are summarized in Table 4.3. A shorter average lifetime ($\boldsymbol{\tau}_{avg}$) was observed for $PbBi_{1.80}Ce_{0.20}Nb_2O_9$ in comparison with pristine PBNO, indicating the introduction of additional non-radiative decay pathways in the Ce-doped

sample. This behavior was attributed to the rapid transfer of photogenerated electrons from the excited states of the PBNO host lattice to the Ce-related electronic states, which act as efficient electron trapping centers (Sriwichai, Sakulsermsuk, Duangjam, Wetchakun and Wetchakun, 2024).

As a result, enhanced charge carrier separation and accelerated interfacial charge transfer were achieved in the optimally doped sample. These effects facilitate the efficient migration of photogenerated electrons and holes toward the surface-active sites of the photocatalyst, thereby promoting effective interactions with MB molecules and leading to improved photocatalytic performance.

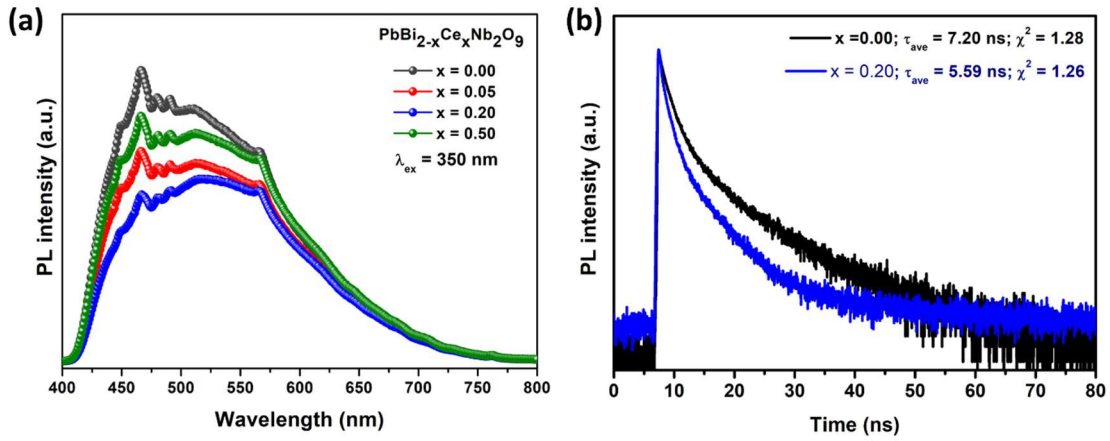


Figure 4.15 PL spectra of $PbBi_{2-x}Ce_xNb_2O_9$ (a) and TRPL spectra of $PbBi_2Nb_2O_9$ and $PbBi_{1.80}Ce_{0.20}Nb_2O_9$ (b).

Table 4.3 TRPL fitted data of $PbBi_{2-x}Ce_xNb_2O_9$ (x=0.00 and x=0.02).

Ce content (x)	Lifetime, τ (ns)			Amplitude (%)			average lifetime, τ_{avg} (ns)	χ^2
	τ_1	τ_2	τ_3	A_1	A_2	A_3		
X=0.00	0.98	2.48	9.83	32.55	41.35	26.10	7.20	1.28
X=0.20	0.49	1.57	6.63	12.26	43.45	44.29	5.59	1.26

To elucidate the generation and contribution of reactive species during the photocatalytic process, potassium iodide (KI) and terephthalic acid (TA) were employed as scavengers for photogenerated holes (h^+) and hydroxyl radicals ($^{\cdot}OH$), respectively. In addition, the influence of dissolved oxygen was evaluated by conducting the photocatalytic reactions under argon (Ar)-saturated conditions. The percentage inhibition of MB degradation over $PbBi_{1.8}Ce_{0.2}Nb_2O_9$ in the presence of various scavengers and under an argon atmosphere is presented in Figure 4.16.

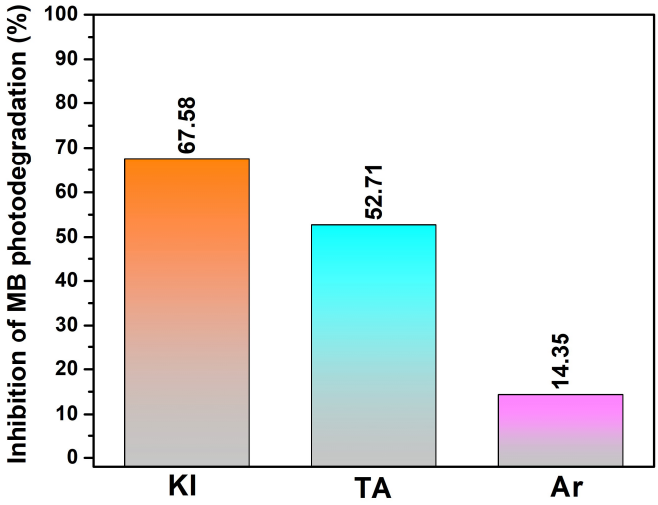


Figure 4.16 Inhibition of MB photocatalytic degradation over $PbBi_{1.8}Ce_{0.2}Nb_2O_9$ in the presence of different scavengers and argon atmosphere relative to the degradation without scavengers and under air atmosphere.

A significant suppression of photocatalytic activity was observed upon the addition of KI and TA, indicating that photogenerated holes (h^+) and hydroxyl radicals ($^{\cdot}OH$) play dominant roles as the primary reactive species responsible for MB degradation. In contrast, only a marginal decrease in photocatalytic efficiency was detected under argon-saturated conditions, suggesting that dissolved oxygen contributes minimally to the overall photocatalytic process. Although dissolved oxygen can act as an electron acceptor and be reduced to form reactive oxygen species such as superoxide radicals ($O_2^{\cdot}-$) and hydrogen peroxide (H_2O_2), its

involvement in the degradation reaction was determined to be secondary compared with that of holes and hydroxyl radicals.

The band potentials of photocatalysts are regarded as critical parameters for determining their redox capabilities under light irradiation. The relative energetic positions of the conduction band (CB) and valence band (VB) edges govern the ability of a photocatalyst to generate reactive oxygen species (ROS), which are essential for the degradation of organic pollutants. To determine the band structure, a combined analysis using X-ray photoelectron spectroscopy (XPS) at the valence band region and UV–vis diffuse reflectance spectroscopy was employed.

The work function (ϕ), defined as the minimum energy required to transfer an electron from the Fermi level (E_F) of a material to the local vacuum level, was estimated using the absolute electronegativity approach (Greiner, Chai, Helander, Tang and Lu, 2012). The absolute electronegativity of a semiconductor was calculated as the geometric mean of the Mulliken electronegativities of its constituent atoms, as expressed by Equation (4.5):

$$\phi = (\chi_A^x + \chi_B^y + \chi_C^z + \cdots)^{1/P} \quad (4.5)$$

where χ denotes the Mulliken electronegativity of each isolated atom, and P represents the total number of atoms in the compound ($P = x + y + z + \cdots$). Based on this method, the work function values were calculated to be 6.14 eV for pristine $PbBi_2Nb_2O_9$ and 6.11 eV for $PbBi_{1.8}Ce_{0.2}Nb_2O_9$, using the Mulliken electronegativity values of Pb (3.90 eV), Bi (4.69 eV), Ce (3.24 eV), Nb (4.00 eV), and O (7.54 eV) (Liao et al., 2022).

The valence band maximum relative to the vacuum level (VBM_{vac}) was determined from valence band XPS spectra (Figure 4.18a and b), which measure the energy difference between the valence band edge and the Fermi level. Subsequently,

the conduction band minimum at the vacuum level (CBM_{vac}) was calculated using Equation (4.6):

$$CBM_{vac} = VBM_{vac} - \mathbf{E_g} \quad (4.6)$$

where $\mathbf{E_g}$represents the optical band gap energy obtained from UV–vis absorption analysis.

To evaluate the photocatalytic redox ability under experimental conditions, the band edge positions referenced to the vacuum level were converted to the reversible hydrogen electrode (RHE) scale using Equation (4.7) (Bard, Faulkner and White, 2022; Trasatti, 1986):

$$\mathbf{E}_{RHE}\ (\text{V at pH}) = -\mathbf{E}_{vac}\ (\text{eV}) - [\mathbf{E_0} + (0.059 \times \text{pH})] \quad (4.7)$$

where $\mathbf{E_0}$is the energy of free electrons on the hydrogen scale, typically taken as 4.44 eV relative to the vacuum level at pH 0.

The relative positions of the valence band maximum and conduction band minimum of $PbBi_2Nb_2O_9$ and $PbBi_{1.8}Ce_{0.2}Nb_2O_9$ with respect to both the vacuum scale and the RHE scale at pH 12 are summarized in Table 4.3. Under alkaline conditions (pH 12), the conduction band potentials of both materials were found to be sufficiently negative to enable the reduction of O_2 to H_2O_2, but not negative enough to promote the formation of superoxide radicals ($O_2^{\cdot -}$). Meanwhile, the valence band potentials were sufficiently positive to oxidize OH^- ions to generate hydroxyl radicals ($^{\cdot}OH$) (Nosaka and Nosaka, 2017). These calculated band edge positions are consistent with the experimental results obtained from active species trapping experiments, thereby validating the proposed photocatalytic mechanism (Dou et al., 2023; Nadolska et al., 2022; Sirusy, Ashrafi and Akhond, 2023).

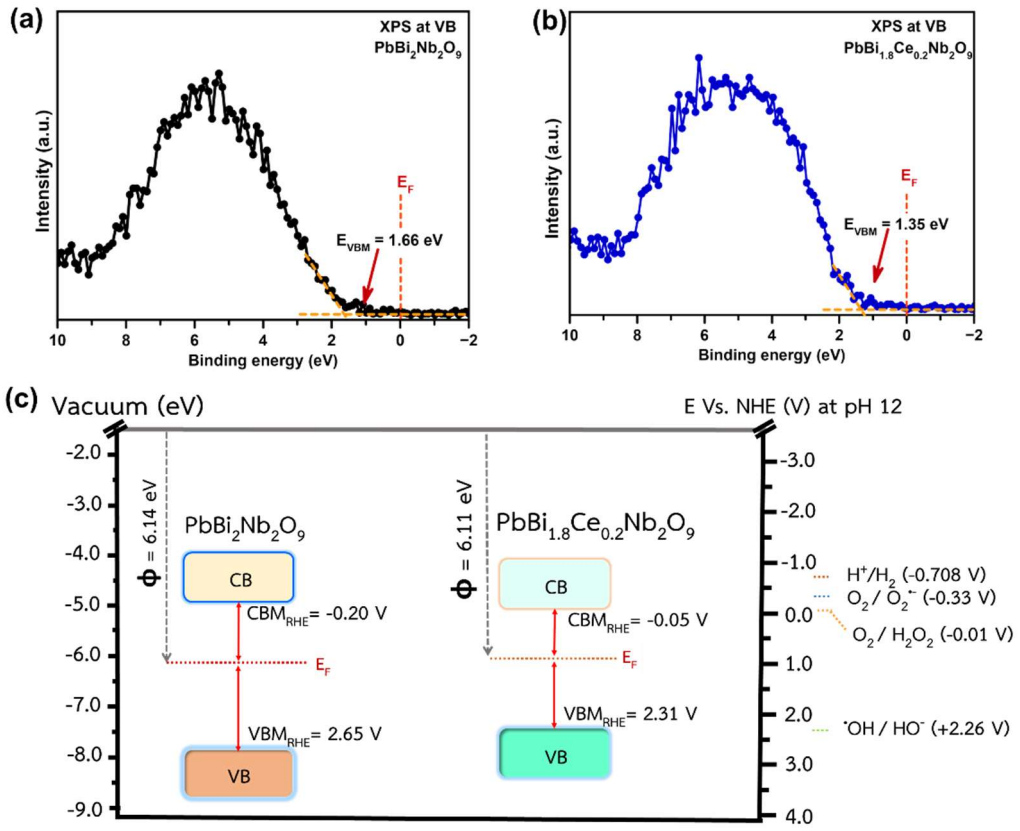


Figure 4.17 XPS at valence band of (a) $PbBi_2Nb_2O_9$ and (b) $PbBi_{1.8}Ce_{0.2}Nb_2O_9$. Diagram of the band energy (c) of $PbBi_2Nb_2O_9$ and $PbBi_{1.8}Ce_{0.2}Nb_2O_9$.

Table 4.4 Band parameters estimated by the calculation of work function (ϕ) and the measurement of UV-vis absorption and XPS valence band spectroscopy.

Compound	ϕ (eV)	E_{VBM} (eV)	E_g (eV)	VBM_{vac} (eV)	CBM_{vac} (eV)	VBM_{RHE} at pH12 (V)	VBM_{RHE} at pH12 (V)
$PbBi_2Nb_2O_9$	6.14	1.66	2.85	-7.80	-4.95	2.65	-0.20
$PbBi_{1.8}Ce_{0.2}Nb_2O_9$	6.11	1.35	2.36	-7.46	-5.12	2.31	-0.05

Accordingly, a photocatalytic reaction mechanism for $PbBi_{1.8}Ce_{0.2}Nb_2O_9$ is proposed based on the experimental results and band structure analysis. As schematically illustrated in Figure 4.18, the incorporation of Ce into the $PbBi_2Nb_2O_9$

lattice is shown to introduce additional electronic energy levels near the bottom of the conduction band, leading to a red shift of the optical absorption edge. As a result, enhanced absorption in the visible light region is achieved, allowing $PbBi_{1.8}Ce_{0.2}Nb_2O_9$ to harvest a broader portion of the solar spectrum. Consequently, an increased number of photogenerated electrons and holes are produced in the conduction band (CB) and valence band (VB), respectively, under light irradiation.

The photocatalytic degradation process of methylene blue (MB) can be described by the following reactions:

$$PbBi_{1.8}Ce_{0.2}Nb_2O_9 + h\nu \rightarrow PbBi_{1.8}Ce_{0.2}Nb_2O_9\ (e^-_{CB} + h^+_{VB}) \quad (4.8)$$

$$h^+ + OH^- \rightarrow HO\bullet \quad (4.9)$$

$$Ce^{4+} + e^- \rightarrow Ce^{3+} \quad (4.10)$$

$$Ce^{3+} + O_2 + H^+ \rightarrow H_2O_2\ (2HO\bullet) \quad (4.11)$$

$$(HO\bullet + h^+) + MB \rightarrow \text{degraded} \quad (4.12)$$

Although various modification strategies have been reported to enhance photocatalytic activity, simple Ce substitution within the PBNO lattice provides multiple synergistic advantages. The incorporation of Ce was found to reduce the band gap energy by modifying orbital hybridization, primarily through the elevation of the valence band maximum without introducing harmful deep-level defect states (Chen, Huang, Wu and Lin, 2012). The upward shift and broadening of the valence band improve charge carrier mobility, while the narrowed band gap promotes efficient photocarrier generation under visible light irradiation.

In addition, photogenerated charge carrier recombination is effectively suppressed by Ce-induced lattice distortions and the presence of Ce^{3+}/Ce^{4+} redox centers, which function as reversible electron trapping sites (Dai et al., 2016). Photogenerated holes are subsequently transported to the catalyst surface, where they react with surface-adsorbed OH^- ions to generate highly reactive hydroxyl radicals ($^{\bullet}OH$) that participate directly in pollutant oxidation (Lin, Kurniawan, Valinton, Chen

and Chuang, 2024). Meanwhile, trapped electrons are transferred to surface-adsorbed oxygen molecules, leading to the formation of H_2O_2, which can further decompose to generate additional $^{\cdot}OH$ radicals, thereby amplifying the oxidative degradation process (Sheng, Li and Xu, 2014).

Furthermore, the increased specific surface area observed in the Ce-doped samples provides a higher density of active sites for photocatalytic reactions. The combined effects of enhanced light absorption, improved charge separation and transport, increased reactive species generation, and enlarged surface area collectively contribute to an approximately 2.6-fold enhancement in the photocatalytic efficiency of $PbBi_{1.8}Ce_{0.2}Nb_2O_9$. This improvement is considered significant when compared with other modification strategies previously reported for $PbBi_2Nb_2O_9$ and related photocatalytic materials, as summarized in Table 4.4.

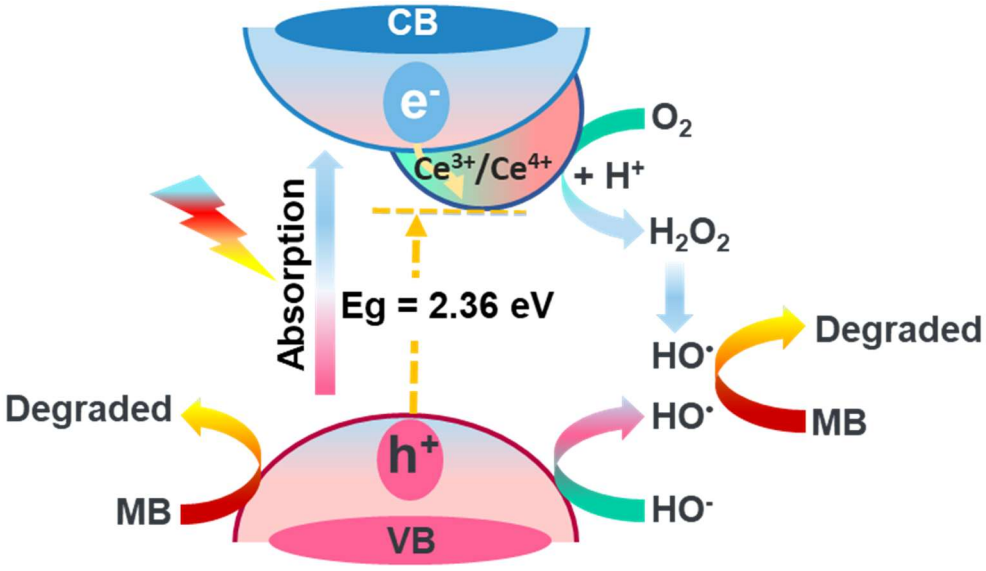


Figure 4.18 Proposed schematic band structures and mechanism of MB photodegradation over the $PbBi_{1.8}Ce_{0.2}Nb_2O_9$ photocatalyst.

4.4 References

Bard, A. J., Faulkner, L. R., & White, H. S. (2022) Electrochemical methods: fundamentals and applications. John Wiley & Sons.

Chen, H.-C., Huang, C.-W., Wu, J. C. S., & Lin, S.-T. (2012). Theoretical Investigation of the Metal-Doped SrTiO3 Photocatalysts for Water Splitting. *The Journal of Physical Chemistry C*. *116*(14), 7897-7903. doi:10.1021/jp300910e.

Chen, X., & Mao, S. S. (2007). Titanium dioxide nanomaterials: synthesis, properties, modifications, and applications. *Chemical Reviews*. *107*(7), 2891-2959.

Chong, M. N., Jin, B., Chow, C. W., & Saint, C. (2010). Recent developments in photocatalytic water treatment technology: a review. *Water research*. *44*(10), 2997-3027.

Dai, Z., Qin, F., Zhao, H., Ding, J., Liu, Y., & Chen, R. (2016). Crystal Defect Engineering of Aurivillius Bi2MoO6 by Ce Doping for Increased Reactive Species Production in Photocatalysis. *ACS Catalysis*. *6*(5), 3180-3192. doi:10.1021/acscatal.6b00490.

Dou, Y., Liang, Z., Xu, Z., Wang, Y., Zheng, J., Ma, D., & Gao, Y. (2023). Composites of Ag-Doped ZnIn2S4 Nanoplates with Graphitic Carbon Nitride and Reduced Graphene Oxide Nanosheets for Sunlight-Driven Hydrogen Production and Water Purification. *ACS Applied Nano Materials*. *6*(13), 12537-12547. doi:10.1021/acsanm.3c02394.

Greiner, M. T., Chai, L., Helander, M. G., Tang, W.-M., & Lu, Z.-H. (2012). Transition Metal Oxide Work Functions: The Influence of Cation Oxidation State and Oxygen Vacancies. *Advanced Functional Materials*. *22*(21), 4557-4568. doi:10.1002/adfm.201200615.

Herrmann, J.-M. (1999). Heterogeneous photocatalysis: fundamentals and applications to the removal of various types of aqueous pollutants. *Catalysis Today*. *53*(1), 115-129.

Hoffmann, M. R., Martin, S. T., Choi, W., & Bahnemann, D. W. (1995). Environmental applications of semiconductor photocatalysis. *Chemical Reviews*. *95*(1), 69-96.

Huang, H., Liu, K., Chen, K., Zhang, Y., Zhang, Y., & Wang, S. (2014). Ce and F Comodification on the Crystal Structure and Enhanced Photocatalytic Activity of Bi2WO6 Photocatalyst under Visible Light Irradiation. *The Journal of Physical Chemistry C*. *118*(26), 14379-14387. doi:10.1021/jp503025b.

Li, Y., Chen, G., Zhang, H., & Lv, Z. (2010). Band structure and photocatalytic activities for H2 production of ABi2Nb2O9 (A=Ca, Sr, Ba). *International Journal of Hydrogen Energy*. *35*(7), 2652-2656. doi:10.1016/j.ijhydene.2009.04.021.

Liao, B., Liao, X., Xie, H., Qin, Y., Zhu, Y., Yu, Y., Fan, X. (2022). Built in electric field boosted photocatalytic performance in a ferroelectric layered material SrBi2Ta2O9 with oriented facets: Charge separation and mechanism insights. *Journal of Materials Science & Technology*. *123*(222-233). doi:10.1016/j.jmst.2022.01.023.

Lin, Y.-C., Kurniawan, A., Valinton, J. A. A., Chen, C.-H., & Chuang, S.-H. (2024). Reduced graphene oxide─MoO3 composites via microwave-assisted synthesis for dual-functional photocatalysis of organic dyes and heavy metal cation under simulated sunlight irradiation. *Journal of the Taiwan Institute of Chemical Engineers*. *154*(105013). doi:10.1016/j.jtice.2023.105013.

Linsebigler, A. L., Lu, G., & Yates Jr, J. T. (1995). Photocatalysis on TiO2 surfaces: principles, mechanisms, and selected results. *Chemical Reviews*. *95*(3), 735-758.

Mizoguchi, H., & Woodward, P. M. (2004). Electronic Structure Studies of Main Group Oxides Possessing Edge-Sharing Octahedra: Implications for the Design of Transparent Conducting Oxides. *Chemistry of Materials*. *16*(25), 5233-5248. doi:10.1021/cm049249w.

Mullins, D. R. (2015). The surface chemistry of cerium oxide. *Surface Science Reports*. *70*(1), 42-85. doi:10.1016/j.surfrep.2014.12.001.

Nadolska, M., Szkoda, M., Trzciński, K., Niedziałkowski, P., Ryl, J., Mielewczyk-Gryń, A., Prześniak-Welenc, M. (2022). Insight into Potassium Vanadates as Visible-Light-Driven Photocatalysts: Synthesis of V(IV)-Rich Nano/Microstructures for the Photodegradation of Methylene Blue. *Inorganic Chemistry*. *61*(25), 9433-9444. doi:10.1021/acs.inorgchem.2c00136.

Nosaka, Y., & Nosaka, A. Y. (2017). Generation and Detection of Reactive Oxygen Species in Photocatalysis. *Chemical Reviews*. *117*(17), 11302-11336. doi:10.1021/acs.chemrev.7b00161.

Sheng, J., Li, X., & Xu, Y. (2014). Generation of H2O2 and OH Radicals on Bi2WO6 for Phenol Degradation under Visible Light. *ACS Catalysis*. *4*(3), 732-737. doi:10.1021/cs400927w.

Sirusy, S., Ashrafi, H., & Akhond, M. (2023). Microtubular Nanoporous g-C3N4@Ag as an Efficient Photocarrier Transfer Agent and Visible Light-Harvesting for Photodegradation of Methylene Blue. *ACS Applied Nano Materials*. *6*(11), 9777-9790. doi:10.1021/acsanm.3c01480.

Somorjai, G. A. (1977) Active Sites in Heterogeneous Catalysis**This work was supported by the U.S. Energy Research and Development Administration. In: Eley, D. D., Pines, H., Weisz, P. B., editors. Advances in Catalysis. Academic Press. p. 1-68.

Soni, S., Vats, V. S., Kumar, S., Dalela, B., Mishra, M., Meena, R. S., Dalela, S. (2018). Structural, optical and magnetic properties of Fe-doped CeO2 samples probed using X-ray photoelectron spectroscopy. *Journal of Materials Science: Materials in Electronics*. *29*(12), 10141-10153. doi:10.1007/s10854-018-9060-x.

Sriwichai, S., Sakulsermsuk, S., Duangjam, S., Wetchakun, K., & Wetchakun, N. (2024). Synergistic effects of Ce and Mo co-doping for enhancing photocatalytic activity of BiVO4 on methyl orange degradation. *Materials Science in Semiconductor Processing*. *184*(108791). doi:10.1016/j.mssp.2024.108791.

Trasatti, S. (1986). The absolute electrode potential: an explanatory note (Recommendations 1986). *Pure and Applied Chemistry*. *58*(7), 955-966.

Vento-Lujano, E., & González, L. A. (2021). Defect-induced modification of band structure by the insertion of Ce3+ and Ce4+ in SrTiO3: A high-performance sunlight-driven photocatalyst. *Applied Surface Science*. *569*(151044). doi:10.1016/j.apsusc.2021.151044.

Watts J, F. (2003). An introduction to surface analysis by XPS and AES. *Chapter*. *5*(149-156).

Yang, S., Shen, H., Cheng, F., Wu, C., Cao, Y., Zhuo, S., Zhang, H. (2020). Organometallic precursor induced defect-enriched mesoporous CeO2 with high specific surface area: preparation and catalytic performance. *Journal of Materials Chemistry A*. *8*(28), 14006-14014. doi:10.1039/D0TA02218G.

Zhang, J., & Nosaka, Y. (2014). Mechanism of the OH radical generation in photocatalysis with TiO2 of different crystalline types. *The Journal of Physical Chemistry C*. *118*(20), 10824-10832.

Zhang, S., Zhao, Y., Díaz-Somoano, M., Yang, J., & Zhang, J. (2018). Synergistic Mercury Removal over the CeMnO3 Perovskite Structure Oxide as a Selective Catalytic Reduction Catalyst from Coal Combustion Flue Gas. *Energy & Fuels*. *32*(11), 11785-11795. doi:10.1021/acs.energyfuels.8b02518.

CHAPTER V
CONCLUSIONS

In this study, $PbBi_2Nb_2O_2$ (PBNO) and Ce-doped $PbBi_{1.8}Ce_{0.2}Nb_2O_9$ photocatalysts were successfully synthesized and systematically investigated to elucidate the effects of preparation methods, calcination temperature, and Ce substitution on structural, electronic, and photocatalytic properties.

The influence of synthesis routes on PBNO revealed that all preparation methods (Sol–gel, Hydrothermal, and Molten salt) produced the desired Aurivillius-type PBNO phase. However, significant differences in crystallinity, morphology, and photocatalytic performance were observed. Although the Molten salt method yielded the highest crystallinity, the Sol–gel-derived PBNO exhibited superior photocatalytic activity toward methylene blue (MB) degradation. This enhancement was attributed to its porous morphology, higher surface area, and defect-rich structure, highlighting that photocatalytic efficiency is not governed solely by crystallinity but also by surface and microstructural characteristics. Consequently, the Sol–gel method was selected for further optimization.

Calcination temperature played a critical role in phase formation and purity. PBNO samples calcined at 750 °C and 800 °C exhibited single-phase Aurivillius structures, while impurity phases were present at lower temperatures. The sample calcined at 750 °C was identified as optimal, achieving high phase purity with reduced energy consumption.

Ce substitution was found to significantly modify the crystal structure, lattice distortion, and electronic properties of PBNO. XRD and Raman analyses confirmed that Ce was successfully incorporated into the PBNO lattice at moderate doping levels (x = 0.20), inducing lattice contraction in the ab-plane, expansion along the c-axis, and increased orthorhombic distortion due to NbO_6 octahedral deformation. Excessive or insufficient Ce doping led to secondary phase formation and structural instability.

Morphological and surface analyses demonstrated that Ce incorporation altered grain growth behavior and increased specific surface area, providing more accessible active sites for photocatalytic reactions. Despite a reduction in long-range crystallinity, Ce-doped samples exhibited improved surface heterogeneity favorable for photocatalysis.

Optical and electronic structure investigations revealed that Ce doping effectively narrowed the band gap and extended light absorption into the visible region. Density of states calculations showed that Ce 4f states contributed to the conduction band minimum, lowering its energy and enhancing visible-light responsiveness. XPS and XAS analyses confirmed the coexistence of Ce^{3+}/Ce^{4+} redox pairs without altering the oxidation states of Pb, Bi, or Nb, indicating that Ce primarily modifies the electronic environment rather than inducing host lattice redox reactions.

Photocatalytic performance evaluation demonstrated that $PbBi_{1.8}Ce_{0.2}Nb_2O_9$ exhibited the highest activity, achieving approximately 2.6 times higher MB degradation efficiency than pristine PBNO under alkaline conditions (pH 12). Kinetic analysis confirmed pseudo-first-order behavior, while cycling tests demonstrated excellent stability and reusability. Photoluminescence and time-resolved PL studies revealed that optimal Ce doping significantly suppressed electron–hole recombination by introducing efficient charge trapping and transfer pathways.

Reactive species trapping experiments and band edge calculations confirmed that photogenerated holes (h^+) and hydroxyl radicals ($^{\bullet}OH$) were the dominant active species responsible for MB degradation, while dissolved oxygen played a minor role. The band structure analysis validated that the valence band positions were sufficiently positive to generate $^{\bullet}OH$ radicals, in agreement with experimental observations.

Overall, the enhanced photocatalytic performance of $PbBi_{1.8}Ce_{0.2}Nb_2O_9$ arises from the synergistic effects of band gap narrowing, improved visible-light absorption, efficient charge carrier separation via Ce^{3+}/Ce^{4+} redox couples, increased surface area, and optimized band edge positions. This work demonstrates that controlled Ce substitution is an effective strategy for improving the photocatalytic efficiency of Aurivillius-type perovskite oxides and provides valuable insights for the rational design of high-performance visible-light-driven photocatalysts for environmental remediation.

CURRICULUM VITAE

Name Mr. Rachanon Klondon

Education 2006-2009 B.Eng. (Chemical Engineering), Suranaree University of Technology

2010-2013 M.Eng. (Chemical Engineering), Suranaree University of Technology

2020-Present Ph.D. candidate (Chemistry), Suranaree University of Technology

International Conference

2024 Oral presentation: Taiwan International Conference on Catalysis, Taipei, Taiwan

Publication

Klondon, R., Waehayee, A., Phonsuksawang, P., Untarabut, P., Wannapaiboon, S., Suthirakun, S., Chen C. H., Siritanon, T. (2025). Band gap reduction in lead bismuth niobate: impact of cerium substitution in aurivillius-type structures on photocatalytic activity. Materials Research Bulletin, 191 (2025), 113541. doi: 10.1016/j.materresbull.2025.113541.